Line profiles of accretion disks around black holes in Schwarzschild-de Sitter and Einstein-Yang-Mills spacetimes

by

Sergei Slobodov

M.Sc., The St.Petersburg Technical University, 1985

A THESIS SUBMITTED IN PARTIAL FULFILMENT OF
THE REQUIREMENTS FOR THE DEGREE OF

MASTER OF SCIENCE

in

The Faculty of Graduate Studies

(Department of Physics and Astronomy)

We accept this thesis as conforming
to the required standard

THE UNIVERSITY OF BRITISH COLUMBIA

September 27, 2003

Department of Physics and Astronomy

The University Of British Columbia
Vancouver, Canada

Date Sep 29, 2003

Abstract

We investigate the characteristic peaks in the iron line profile in the black hole accretion disk X-ray spectrum in two static spherically symmetric metrics, Schwarzschild-de Sitter metric and the Einstein-Yang-Mills black hole metric.

For the Schwarzschild-de Sitter metric our results show that for a fixed mass black hole, the peaks become less pronounced and closer together with increasing cosmological constant Λ. This effect is mainly due to the slower rotational velocity of Keplerian orbits at large radii in the Schwarzschild-de Sitter spacetime as compared to that for the Schwarzschild spacetime. This change of the iron line profile is similar to that obtained from extending the accretion disk size or reducing the emission power law exponent in the Schwarzschild black hole accretion disk models. Based upon the current estimates of Λ, black holes of at least 10^{18} solar masses are required to make the effect observable.

For Einstein-Yang-Mills black holes, the line profiles depend strongly on the horizon radius and the solution number n. For $n = 1$ the profile is similar to that of a Schwarzschild black hole. In contrast, the shallow slope of the g_{00} component of the metric for $n = 2, 3, 4$ solutions increases the line width for these solutions significantly, in some cases creating a second pair of peaks redshifted approximately by a factor of 2, breaking the usual correspondence between the position of the blue peak and the black hole mass. The line profiles of solutions for $n = 5 - 8$ and higher, depending on the horizon radius, closely resemble that of extreme Reissner-Nordstrom black hole. In addition, due to an island of orbit stability near the Einstein-Yang-Mills black-hole horizon for the solutions with small horizon radius r_h, there is an extra pair of peaks in the line profile redshifted by a factor of 30 times or more relative to the main line. These features might be used to distinguish accreting Einstein-Yang-Mills black holes from Schwarzschild and Kerr black holes.

Contents

List of Tables

List of Figures

Acknowledgements

The two years of my Masters program have been especially rough on my wife Maria and I thank her for the many ways she has been keeping our family together during this time. My thanks to my old friend Dr.Vlad Snetkov of King's College of London, whose visit to Vancouver in March 2001 eventually led to my decision to go back to school after a 16-year break. I thank Dr.Kristin Schleich for taking a chance and agreeing to be my M.Sc. supervisor and helping me every step of the way, and especially during the tough first term. I'm grateful to Janet Johnson, the graduate secretary of the UBC Physics and Astronomy Department at the time of my application, who encouraged me to apply despite the tight time constraints. I thank Dr.Matthew Choptuik for patiently answering my questions on numerical analysis and on meaning of my results. I also thank many fellow graduate students who helped me figure out answers to some tough (for me, anyway) problems, especially Henry Ling and Phil DeBoer, and Roman Petryk and Bruno Rousseau for lending me the textbooks I was too cheap to buy.

Introduction

Observing the iron K_α line in X-ray fluorescence emitted from the accretion disk around a black hole is an attractive way to probe the geometry of spacetime in this region, because this normally narrow line is seen by a remote observer as a characteristic two-peak profile fluorescence spectrum [8],[25]. This profile carries the imprint of the spacetime metric in the vicinity of the emitting region; the curvature of spacetime affects this line both by Doppler broadening from the moving scatterer in the accretion disk and by gravitational redshift of the scattered photons. Quantitative calculations of this iron line profile have been previously obtained for two natural choices of black hole backgrounds: the Schwarzschild and Kerr solutions (see e.g. [5], [8], [9], [15]). The resulting spectra are qualitatively the same, but are potentially observationally distinguishable with high resolution spectral observations. In recent years, with the launch of Chandra and XMM-Newton, the quality of the observed spectra is beginning to approach the resolution necessary to discriminate between these two background spacetimes [1]. It is natural to ask whether or not other background spacetimes will produce identifiable features in precision measurements of iron line profiles. In this thesis we will consider two such spacetimes: one with the cosmological constant and one with the Einstein-Yang-Mills (EYM) fields.

We begin by reviewing the necessary formalism for the calculation of the spectrum of a narrow emission line in a static spherically symmetric metric. This is the subject of chapter 1. In section 1.2 we describe our algorithm, which is based on the method given in [4] for numerically computing the spectra. In chapter 2 we apply this formalism to a vacuum metric with non-zero cosmological constant and study the effects of the cosmological constant Λ on the line shape of the accretion disk spectra. In section 2.2 we present our calculated line profiles. We find that the cosmological constant modifies the line profile; however, for the currently accepted range of the cosmological constant values, $\Lambda = (0.71 \pm 0.03)\Omega_{vac}/\Omega_{crit}$, where Ω_{vac} and Ω_{crit} are the vacuum energy density and the critical[1] density respectively, this effect is only observable if the black hole is unrealistically massive, 10^{18} solar masses. Alternately, for black holes in galactic cores with masses of 10^6 to 10^8 solar masses, a cosmological constant 20 or more orders of magnitude greater than the currently accepted value is needed to produce a noticeable effect.

We next turn to the emission spectra of accretion disks of spherically-symmetric SU(2) Einstein-Yang-Mills (EYM) black holes. This research is described in chapter 3. The solutions pf the coupled Einstein-Yang-Mills equations attracted considerable interest after Bartnik and McKinnon had numerically discovered regular solutions ([2]). Section 3.1 reviews the regular and black-hole asymptotically-flat EYM solutions, section 3.2 describes our implementation of the algorithm of numerically finding EYM solutions and presents

[1] Corresponding to the spatially flat Universe

such solutions and their properties. The computed line profiles are presented in section 3.5. We found that the line profiles for EYM black holes with the horizon radius $r_h \geq 1$ are similar to the Schwarzschild line profiles for the solution number $n = 1$, and are close to the maximally-charged (extreme) Reissner-Nordstrom (spherically symmetric black holes with electric charge $Q = M$ in appropriate units) for $n = 5$ and up, but have a number of additional features for $n = 2, 3, 4$, due to the form of the metric function g_{00}. For $r_h << 1$, where the repulsive Yang-Mills contribution is very strong, the metrics and line profiles converge to the extreme Reissner-Nordstrom solution only at $n = 7$. An additional phenomenon in the EYM metrics with small horizon radius is the existence of a range of stable timelike circular orbits near the horizon. Emission from these orbits contributes to the line profile as a weak two-peak feature strongly red-shifted by a factor of 30 or more.

Throughout this work we use units where $G = 1$ and $c = 1$, for brevity.

Chapter 1

Line Profile Calculation Basics

A large amount of information about black hole accretion disks is accessible to us through the analysis of the disk spectrum, or in astronomical terms, its line profile. Light emitted from the disk is Doppler-shifted due to disk rotation as well as gravitationally redshifted and lensed by the strongly spacetime curvature near the black hole. Total frequency shift depends on the emitter position in the disk, and so a narrow emission line looks broadened to the remote observer. Energy flux measured at a given frequency comes from all parts of the disk that would appear to the observer to emit at that frequency. Thus the overall line profile carries the information about the metric, which can be extracted by comparing observed profiles with those predicted by models.

Of all the processes that may result in light emission from accreting black holes we choose just one: the iron K_α emission due to the accretion disk fluorescence [8]. This process results in X-ray emission with a very narrow 6.4 keV line. This is a strongest line in this region and is a good nearly-monochromatic light source in the emitter frame, such that any observed change of this line can be attributed to the effects of the metric near the central object. For simplicity, we always work in the geometric optics approximation, i.e. we assume that the size of the black hole and its disk is much greater than wavelength of the emitted light. This implies that the emitted light rays travel along null geodesics. This approximation is valid for a broad range of black holes, given that wavelength of the K_α line is many orders of magnitude smaller than the typical stellar black hole size. There are many approaches to analytically and or numerically modeling accretion disk line profiles: [4, 5, 6, 8, 9]. We follow that of Chen and Eardley, [4], with minor modifications, as we find it intuitive and easily generalized to an arbitrary static spherically symmetric metric.

Similarly, we assume that the disk consists of test particles, non-interacting point-like objects with negligible mass traveling along circular time-like geodesics (Keplerian orbits) along a single thin rotation plane, and emitting a great deal of X-ray radiation. Some of these assumptions are more justifiable than others. Ignoring the effects of the surrounding disk on the metric formed by the black hole is reasonable for many accretion models, as the disk mass is much smaller than that of the central object. The Keplerian nature of the motion of the particles is much less certain, given the strong magnetohydrodynamic effects likely taking place in the disk. It is also likely that the disk may be inhomogeneous, anisotropic, non-stationary and thick. See [8] for the discussion of these assumptions. All these factors, while very important in the study of accretion disks, are ignored in the first approximation, as our goal is the study of feasibility of discerning the non-Schwarzschild features of the metric using accretion disk line profile.

1.1 Calculating Observed Line Profile

To calculate the observed spectrum from an accretion disk as a whole, we need to add the flux reaching the remote observer from every infinitesimal element of the disk. As each part of the disk is at a different position in the curved spacetime, different parts of the disk would have different color and brightness, from the observer's point of view. Since the disk is too far to be seen as anything other than a point-like source, the line profile is the sum of the flux from each point in the disk emitting at a given frequency towards the observer. We now proceed to calculate this flux.

The frequency shift g of a photon traveling from emitter to observer is given by

$$g = \frac{\nu}{\nu_e} = \frac{-p \cdot u_o}{-p \cdot u_e}, \tag{1.1}$$

where ν_e is the frequency of the photon in the emitter's frame, ν is the frequency of the photon as measured by the observer, p is the 4-momentum of the photon along its null geodesic and u_{obs} and u_{em} are the 4-velocities of the observer and the emitter respectively.

One should distinguish between the differential flux at a given frequency and the bolometric flux, integrated over the whole range of frequencies. The total bolometric flux F seen by an observer is linked to that emitted from the source by a factor of g^4 due to conservation of 4-volume [18]. Hence, the observed and emitted intensities at a given frequency are related to each other by a factor of g^3.

The observed line flux at a given frequency from the accretion disk can be readily expressed in terms of the specific intensity $I(\Omega, r, \nu_e)$ in the emitter's frame and the frequency shift g:

$$F_\nu = \int g^3 I(\Omega, r, \nu_e) d\Omega, \tag{1.2}$$

where the integration is over the angles subtended by the disk image. Note that F_ν will depend on the inclination of the disc relative to the line of sight of the observer.

To proceed further, explicit expressions for the intensity and frequency shift are necessary; we will derive them first for a general static, spherically symmetric metric. These calculations can be considerably simplified by a convenient choice of the coordinates. Following [4], we use a spherical coordinate system (t, r, θ, ϕ) centered around the gravitational source and z-axis pointing towards the observer. Further, without loss of generality, we choose the accretion disk axis to be in the $y = 0$ plane, with the axis projection towards negative x. (See Fig. 1.1, based on Fig.1 of [4].) The inclination angle i is the angle between z-axis and the disk axis.

The general static spherically symmetric metric can be written in these coordinates as

$$ds^2 = -T(r)dt^2 + R(r)^{-1}dr^2 + r^2 d\Omega^2. \tag{1.3}$$

Note that spherical symmetry implies that all geodesics will be planar. The 4-velocity of a circular timelike geodesic in the accretion disk at the radial coordinate r in this metric is (see Appendix A.1 for derivation)

$$u_e^a = \gamma(t^a + \frac{1}{r} v \cos\alpha \theta^a + \frac{1}{r \sin\theta} v \sin\alpha \phi^a) \tag{1.4}$$

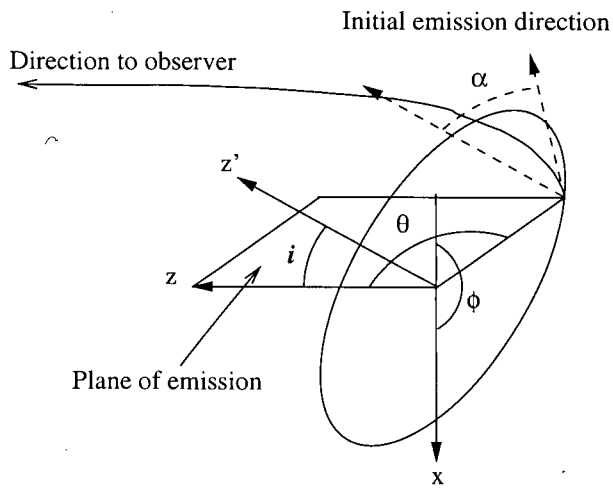

Figure 1.1: Emission angle α and inclination angle i in the spherical coordinate system of the observer (1.3). Here z is the observer's z-axis, z' is the accretion disk's axis, x is the x-axis in either coordinates and i is the disk inclination.

where $\gamma = (T - v^2)^{-\frac{1}{2}}$, $v = \sqrt{\frac{rT'}{2}}$. t^a,r^a, θ^a and ϕ^a are the coordinate basis vectors and α is the angle between the plane of the disk and the plane defined by the emitting point, the center of the disk and the observer. This angle can be expressed in terms of i and ϕ as

$$\cos\alpha = \sin i \sin\phi. \tag{1.5}$$

The polar angle of the intersection in these coordinates is given by

$$\cot\theta = \cos\phi \tan i; \tag{1.6}$$

The 4-momentum of a photon emitted from the accretion disk (see Appendix A.2 for derivation) is

$$p^a = h\nu(\frac{1}{T}t^a + \sqrt{\frac{R}{T} - R(\frac{b}{r})^2}\, r^a + \frac{b}{r^2}\theta^a). \tag{1.7}$$

where b is the photon impact parameter. The corresponding null geodesic lies in the plane connecting the observer, the emitter and the center of the disk.

In general, the remote observer's 4-velocity would depend on the choice of the observer. It is easy to see that the dependence of the accretion disk spectrum on the observer's 4-velocity is limited solely to an overall frequency shift factor. Thus, for an investigation of the line shape we can choose any observer we like. The position of the observer relative to the disk, described by the disk inclination is what's really important, because it determines the direction in which the light has to be emitted to hit the disk, relative to the emitter's direction. This affects both the frequency shift and the observed flux in a way that heavily depends on where in the disk the emitter is. So the numerator in the expression (1.1) serves as a normalization point only, and can usually be ignored. We illustrate this point by considering two natural choices for the 4-velocity u_o of a timelike observer in a spherically

symmetric metric: that corresponding to an observer maintaining a fixed distance d from the black hole,

$$u_o^a = \frac{1}{\sqrt{T(d)}} t^a \tag{1.8}$$

and that corresponding to a radially freely falling observer at distance d,

$$u_o^a = \frac{\epsilon}{T(d)} t^a \pm \sqrt{\frac{1}{R(d)}(\frac{\epsilon^2}{T(d)} - 1)}\, r^a \tag{1.9}$$

where ϵ is a constant determined by the initial radial velocity. Note that if the spherically symmetric metric is not asymptotically flat, (1.8) will not approach the timelike killing vector t^a for large d. These two 4-velocities coincide for the choice of zero radial velocity at d, $\epsilon = T(d)$. In the following we will use (1.9).

The frequency shift is conveniently written in terms of two factors:

$$g = g_{obs} g_{disk}, \tag{1.10}$$

where for a given photon impact parameter b, g_{obs} depends on d and ϵ only,

$$g_{obs} = \frac{\epsilon}{T(d)} - \sqrt{\frac{1}{T(d)}(\frac{\epsilon^2}{T(d)} - 1)}\sqrt{1 - T^2(d)\frac{b^2}{d^2}} \tag{1.11}$$

and the expression for g_{disk} depends on the emitter's position r only:

$$g_{disk} = \frac{1}{\gamma(1 - \frac{b}{r} v \sin i \sin \phi)}. \tag{1.12}$$

We will assume that the iron line emission in the emitter's frame is monochromatic and isotropic with no local line broadening. For this case the dependence on radius r of the specific intensity is commonly modeled by a power law dependence. Assuming an optically thin disk,

$$I(\Omega, r, \nu_e) = \frac{\kappa}{4\pi\mu'} r^{-p} \delta(\nu_e - \nu_0). \tag{1.13}$$

The power p is usually taken to be in the range of $1 \to 3$; κ is a constant with units of power. The factor μ' is the cosine of the angle between the emitted photon and the disk axis in the emitter's frame,

$$\mu' = \frac{gb \cos i}{r \sin \theta}. \tag{1.14}$$

An explicit derivation of the form μ' in the observer's coordinates is given in ref. [5].

The infinitesimal solid angle subtended by the disk is easily expressed in terms of the impact parameter b and ϕ:

$$d\Omega = \frac{bdbd\phi}{d^2} \tag{1.15}$$

Combining terms and re-expressing $\nu_e = \nu/g$ in (1.13) we have

$$F_\nu = \frac{\kappa}{4\pi d^2} \int g^3 \frac{r \sin\theta}{b \cos i} r^{-p} \delta(\nu - g\nu_0) b db d\phi \tag{1.16}$$

using the identity $\delta(\nu/g - \nu_0) = g\delta(\nu - g\nu_0)$. The range of integration is over ϕ and b such that the null geodesics intersect the disk. The coordinates r, θ of the intersection point are implicitly a function of b, ϕ, and i; a null geodesic of given b and ϕ will intersect the accretion disc at angle i at a given r and θ. For a given frequency v, contributions to F_v are from points on the accretion disk with equal value of g (See [17] Fig.7 for an example of such contours for Schwarzschild.). Observe that the intersection of the null geodesic with the accretion disc can occur either before or after the turning point.

1.2 Numerical Spectrum Calculation

Each emission point of the accretion disk "seen" by a remote observer corresponds to a distinct pair of impact parameter and polar angle (b, ϕ). Thus sampling the (b, ϕ) space is equivalent to sampling the whole disk. This approach, due to [4], circumvents the need to explicitly evaluate the Jacobian of coordinate transformation from the disk coordinates to observer coordinates. In other approaches ([6, 8, 9]) this Jacobian is calculated either numerically or analytically.

An easy way to determine the emission point in the disk (r, ϕ) that corresponds to the image point (b, ϕ) is to extend a null geodesic from infinity to the point where it intersects the disk. The usual way of numerically integrating the null geodesic is to use second-order geodesic equations in order to avoid complications near turning points(see, for example, [17, 18]). There are also ways to use first order methods without having to worry about turning point by applying a clever variable substitution ([4]). We chose to integrate the differential equation of null geodesic

$$\frac{dr}{d\theta} = \pm r \sqrt{R(\frac{(\frac{r}{b})^2}{T} - 1)}, \tag{1.17}$$

directly by a first order method and deal with the turning point explicitly. We use a small fixed angular increment $d\theta$ (typically 0.2°) and calculate the radial increment dr from the equation 1.17. We adjust angular increment to limit the radial step to $0.1r$, which is usually required for the initial and final phases of null geodesics, where fixed $d\theta$ corresponds to very large radial steps. To produce a "bounce" from the turning point, we change the sign of $\frac{dr}{d\theta}$ from $-$ to $+$ when the argument of the square root becomes negative. This first order method is stable under changes in angular step size and reproduces certain analytic deflection results to high accuracy. Figure 1.3 shows null geodesics for the Schwarzschild metric obtained for three different angular step sizes $d\theta = 2°, d\theta = 0.2°, d\theta = 0.02°$.

One can see that even for a very coarse-grained angular discretization the accuracy of the results is quite good (the accumulated total angular error is only about 3° for the worst case with 2° angular step). Similar results were obtained for the extreme Reissner-Nordstrom

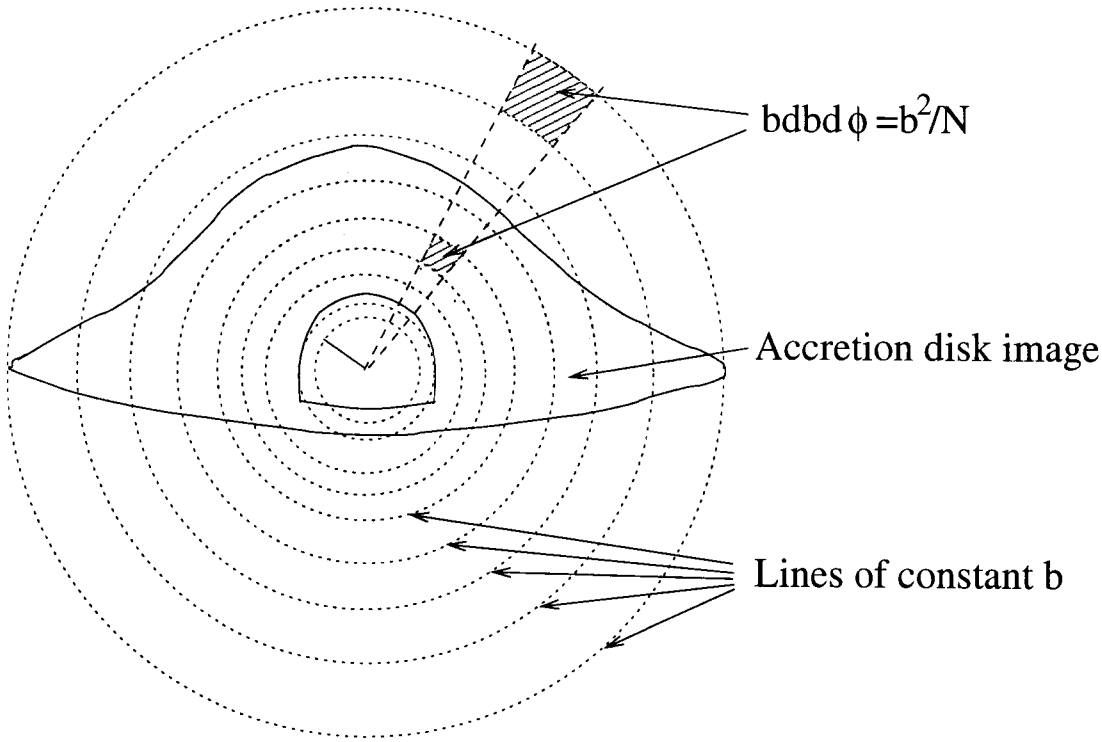

Figure 1.2: For numerical calculations the accretion disk image is divided into N^2 nearly square elements whose boundaries are lines of constant b and constant *phi*. The area of each element is chosen to be proportional to the square of b.

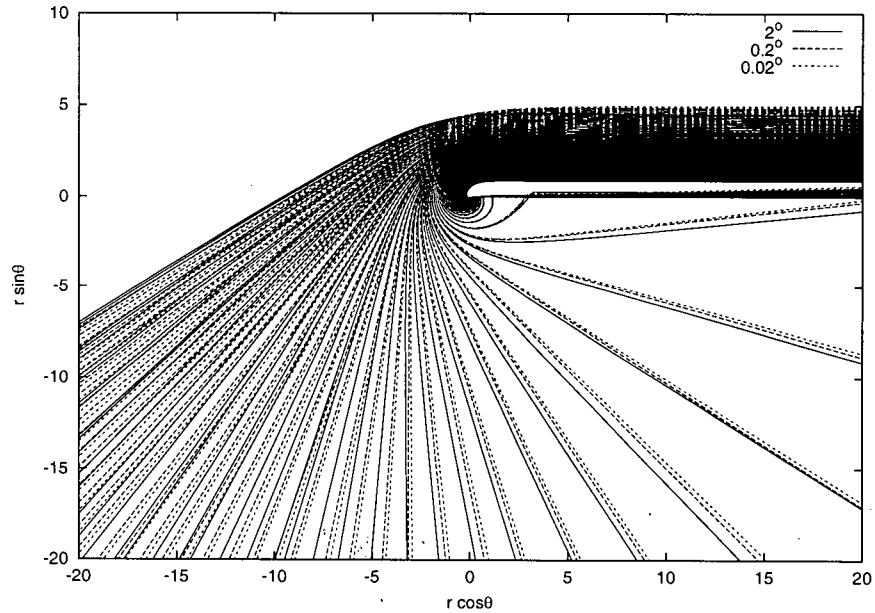

Figure 1.3: Dependence of numerically computed null geodesics for Schwarzschild metric on the angular step magnitude.

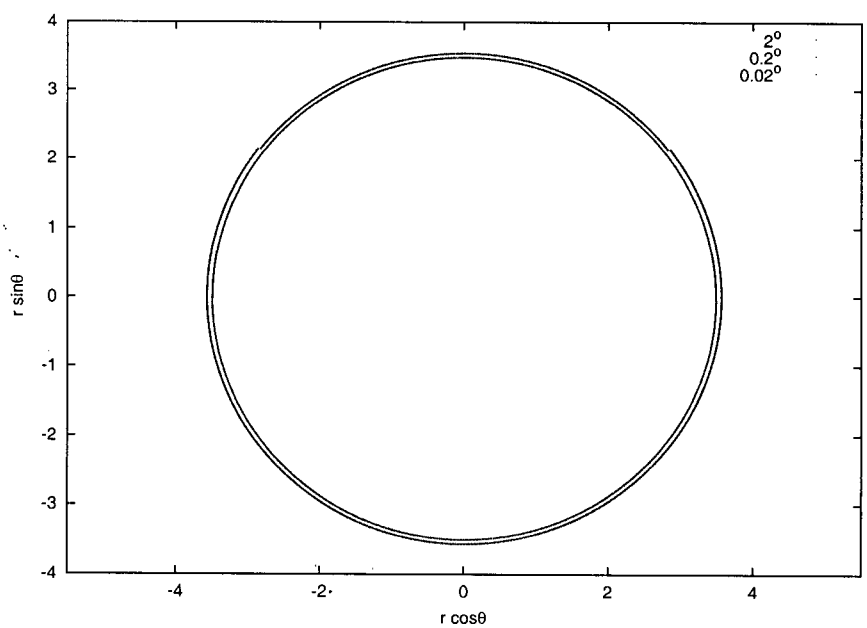

Figure 1.4: Effects of geodesic discretization on ring image appearance. Coarse discretization results in larger and rougher disk image. There is no observed difference once the angular step is 0.2° or better.

and the EYM metrics as well. One can also see the effects of geodesic discretization by looking at an image of a thin ring obtained by plotting all (b, ϕ) pairs for which geodesics hit the ring, as shown on figure 1.4. One can see that the $d\theta = 2°$ discretization produces a larger ring image. Also, since we used linear interpolation to fill the gap between adjacent numerically calculated (r, θ) points when calculating the disk intersection points, the edges of the ring image look somewhat rougher for the coarser step size. There is no observable difference between the ring images for step sizes of 0.2° and 0.02°.

The spectrum calculation algorithm is as follows:

1. Specify the metric and the disk parameters: the desired number of disk image elements to use, the inner and outer disk radii in dimensionless units, r_{in}, r_{out}, the inclination angle i of the disk and the emission intensity power law exponent p(see 1.13).

2. Sample the (b, ϕ) space. To accomplish this, we discretize $d\phi = 2\pi/N$ and take $db = 2\pi\ b/N$. The impact parameter b ranges from zero to a value determined by the outer disk radius, chosen so that no null geodesic with greater b will intersect the disk. The flux contribution from each element and its frequency shift is taken to be that of center of each element.

3. For each sample point, integrate the null geodesic from the observer to the disk to the point where it intersects the disk (the emission point). (Points in (b, ϕ) with null geodesics found not to intersect the disk at this step are discarded.)

4. Calculate the frequency shift using equation (1.12) and the spectral flux from the disk element using equation (1.16). Add the resulting intensity to the appropriate frequency point of the spectrum.

To implement the line profile calculation algorithm we chose to use a programming language with low run-time performance overhead (C in our case, FORTRAN could have been used as well), rather than higher-level formula-based languages, such as those built in Mathematica or Maple. This is because of the concerns for run time demands. On average we had to calculate about $10^6 \ldots 10^7$ geodesics for each line profile to get a smooth picture. This number of points took several seconds of computer processing time to complete. Some line profiles, such as those with very high or very low inclinations, or with very large outer radius, required up to 10^9 points. In these cases the calculation time could be as high as an hour or longer.

Note that we modeled the disk image as a collection of small nearly-square elements in the space (b, ϕ), as shown on Fig. 1.2, and calculate the flux from each one, assuming uniform flux from each piece. The error introduced by this procedure adds noise to the resulting line profile. Figures 1.5, 1.6, 1.7 show the convergence to a smooth profile in different cases. Higher noise level for the same discretization is seen for large outer radii, for high inclination angle, or for lower emissivity power p. This is because, for a given number of disk elements, fewer of the image elements overlap the important inner disk area for a large disk. This effect is masked somewhat for lower p because of smaller contribution from the outer layers in our discretization scheme. Similarly, for a large

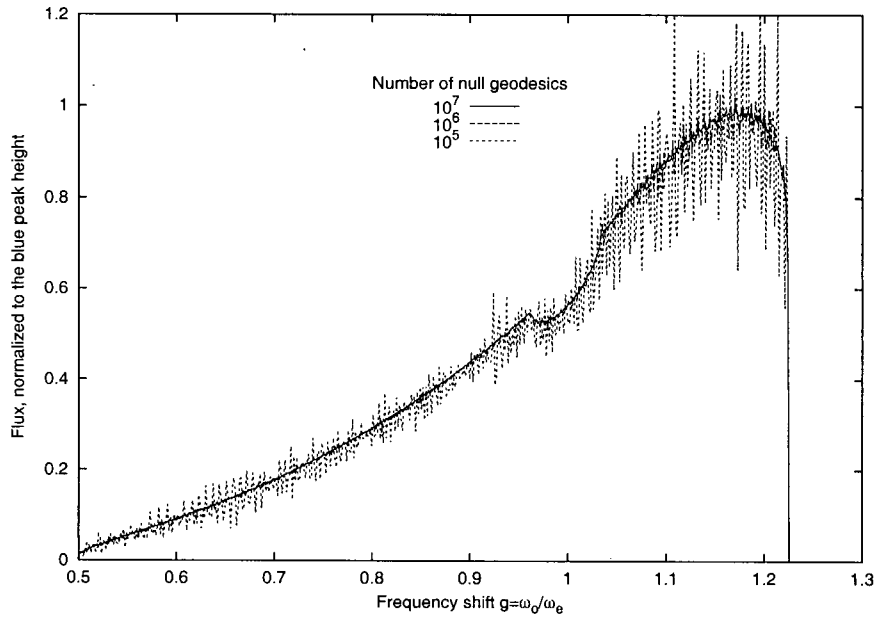

Figure 1.5: Effects of disk image discretization on line profile smoothness. Model parameters: Schwarzschild metric with horizon radius $r_h = 1$, disk geometry: $i = 60°$, $r_{min} = 3$, $r_{max} = 300$, $p = 3$. Good results require only 10^6 points. Line profiles are scaled to coincide.

inclination angle, fewer elements overlap the disk, causing a higher noise level. Also in this case a nearly square element in the image maps to a significantly distorted area of the disk. However, we observed no measurable systematic error even for significant discretization noise. Our solution was to increase the number of points (and correspondingly the line profile computation time) from the usual choice of 10^7 to 10^8 or even to 10^9 in such cases. Alternatively, one could discretize the disk itself, rather than the disk image, then calculate the impact parameter corresponding to each disk element by finding a geodesic that reaches the observer. This approach is taken in a number of papers ([7, 8, 9]). There will be no difference in the final line profile, provided the disk/image discretization is fine enough.

1.3 Results for Schwarzschild Metric

For algorithm verification purposes, we run the simulations for the Schwarzschild metric. Figures 1.8 and 1.9 show the disk images we generated for the Schwarzschild metric for two different disk inclinations. These correspond to the images originally generated by Luminet in [17], Fig.6.

We next calculated line profiles for the Schwarzschild case with the parameter sets taken from [8] Fig.1, [4] Fig.4a-7a[1]. Our simulation results are generally indistinguishable from

[1]The captions of [4] Fig.4 and Fig.6 appear to be swapped in print.

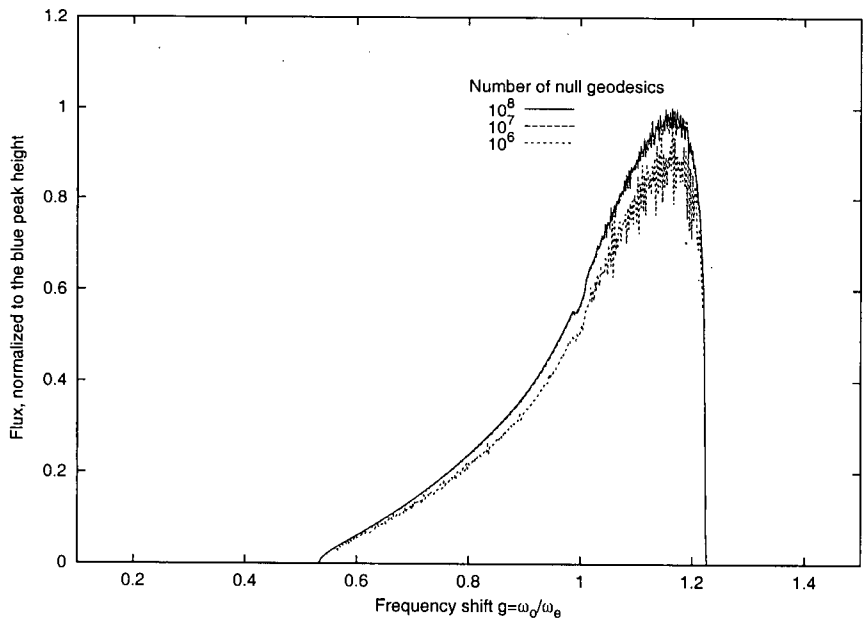

Figure 1.6: Effects of disk image discretization on line profile smoothness. Model parameters: Schwarzschild metric with horizon radius $r_h = 1$, disk geometry: $i = 60°$, $r_{min} = 3$, $r_{max} = 3000$, $p = 3$. Good results require at least 10^8 points. Line profiles are scaled differently to allow visual comparison.

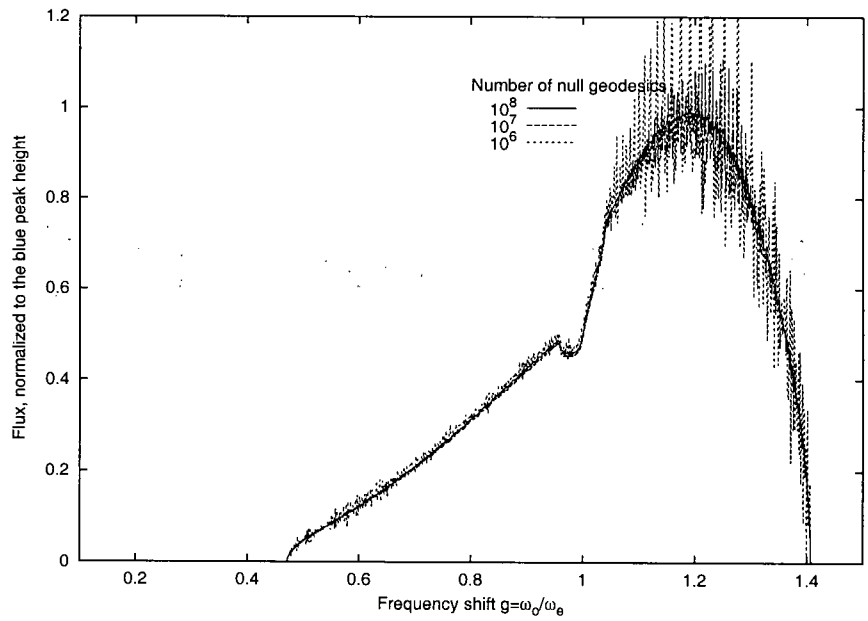

Figure 1.7: Effects of disk image discretization on line profile smoothness. Model parameters: Schwarzschild metric with horizon radius $r_h = 1$, disk geometry: $i = 85°$, $r_{min} = 3$, $r_{max} = 3000$, $p = 3$. Good results require at least 10^8 points. Even 10^8 point-run does not get rid of the discretization noise completely. Line profiles are scaled to coincide.

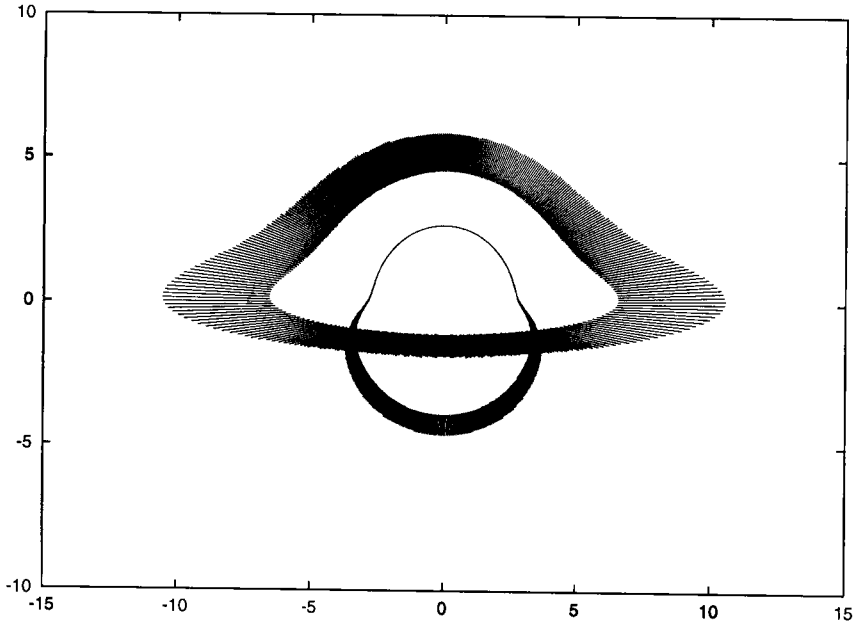

Figure 1.8: Image of an accretion disk around a Schwarzschild black hole with the horizon radius $r_h = 1$. Disk inner radius is the radius of marginal stability $r_{ms} = 3$ and the outer radius is $r_{out} = 10$. Disk inclination is $i = 10°$.

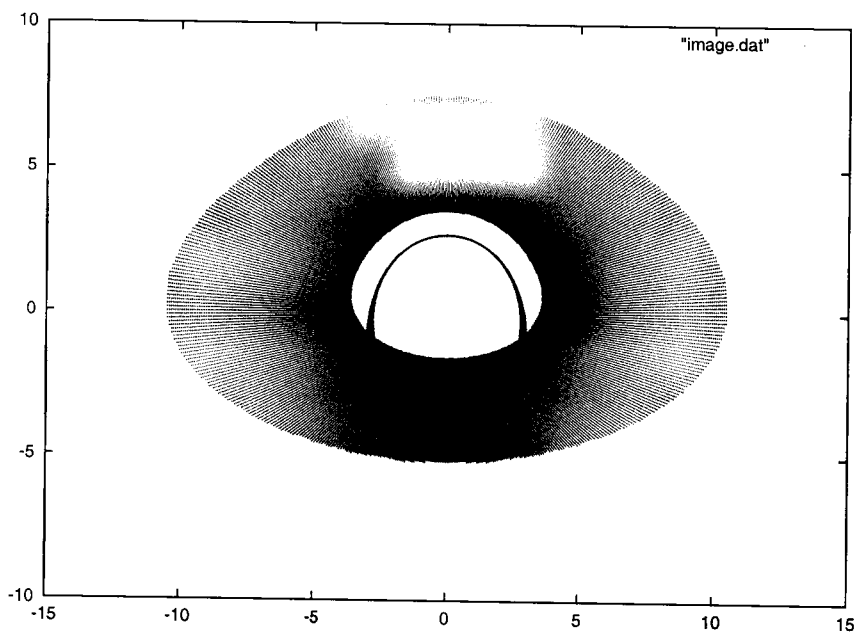

Figure 1.9: Image of an accretion disk around a Schwarzschild black hole with the horizon radius $r_h = 1$. Disk inner radius is the radius of marginal stability $r_{ms} = 3$ and the outer radius is $r_{out} = 10$. Disk inclination is $i = 30°$.

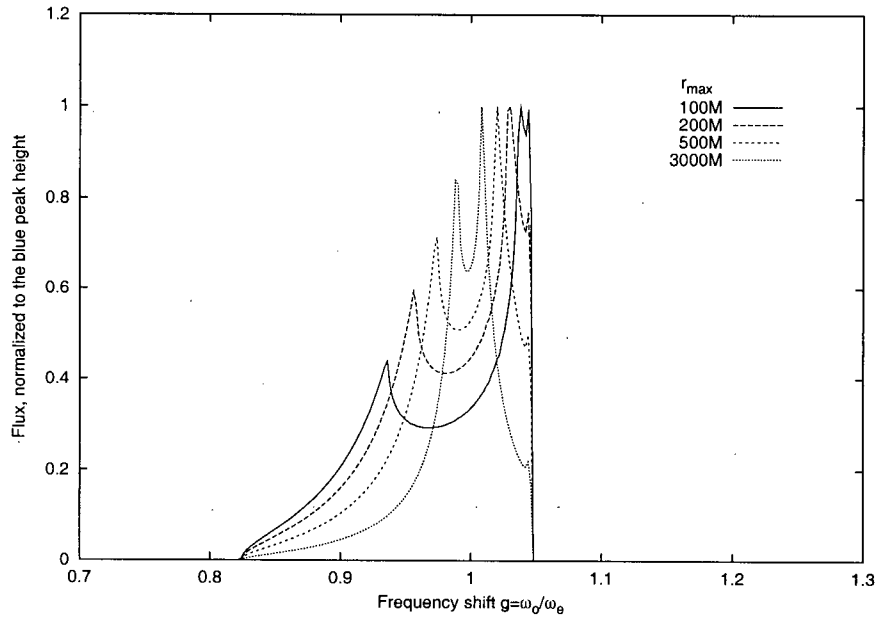

Figure 1.10: Spectra calculated for the Schwarzschild metric with parameters taken from [8] Fig.1b: $i = 30°$, $p = 2$, $r_{min} = 20M$, $r_{max} = 100M, 200M, 500M, 3000M$ (left to right).

those in the original papers. For example, a set of line profile spectra calculated using the parameters taken from Fig.1b of [8] is shown on Fig. 1.10 and replicates the spectra from that paper. We feel confident that our implementation of the accretion disk fluorescence spectrum calculations is solid enough to apply it to other interesting cases.

In the pure Schwarzschild case, the line profile of the black hole normalized to the height and position of the blue peak, does not depend on the mass M of the black hole. Instead, it depends on three dimensionless parameters: the ratios of the inner and outer accretion disk radii to the black hole mass and the emissivity parameter p. The emissivity parameter p determines the sensitivity of the line profile to the outer disk radius. The line profile for $p = 2$ ([8]) is more sensitive to the choice of outer radius than that for $p = 3$ ([4]); this is easily understood, as the total flux from a radius r and assuming a constant frequency shift falls off as r^{2-p}, and so the observed contribution from the outer parts of the disk for $p = 3$ falls off approximately as $\frac{1}{r}$. The full width of the line is determined by the innermost parts of the disk for a significantly inclined disk. This can be seen by looking at the frequency shift formula 1.12 applied to the Schwarzschild case:

$$g_{disk} = \frac{\sqrt{1 - \frac{3M}{r}}}{1 - \frac{b}{r}\sqrt{\frac{M}{r}} \sin i \sin \phi}. \tag{1.18}$$

Here the numerator (gravitational red shift) varies between $\frac{1}{\sqrt{2}}$ and 1, while the denominator at the innermost stable orbit $r = 6M$ varies between $\frac{1}{2}$ and $\frac{3}{2}$ for a maximally inclined disk,

restricting the line profile to between 0.47 and 1.41 of the emitted frequency.

Chapter 2

Line Profiles in Schwarzschild-de Sitter metric

2.1 Schwarzschild - de Sitter Metric

The results of the previous chapter can be applied to the Schwarzschild-de Sitter (SdS) metric. This metric describes a static spherically symmetric vacuum solution of Einstein equations with cosmological constant. Cosmologically, this is a good model of an isolated black hole in a dark energy-dominated spatially flat universe. The Schwarzschild - de Sitter metric in static coordinates is

$$ds^2 = (1 - \frac{2M}{r} - \frac{1}{3}\Lambda r^2)dt^2 + \frac{dr^2}{1 - \frac{2M}{r} - \frac{1}{3}\Lambda r^2} + r^2 d\Omega^2 \,. \tag{2.1}$$

Before proceeding, we first look at the causal structure of this spacetime, since the metric functions $T(r) = R(r) = 1 - \frac{2M}{r} - \frac{1}{3}\Lambda r^2$ become negative at large enough values of r, violating the assumptions stated in appendix A.1. The metric (2.1) describes one part of the maximal extension of the Schwarzschild-de Sitter spacetime. A Penrose-Carter diagram for the covering SdS spacetime may consists of any number of patches shown on the figure 2.1, stitched together and/or identified along their left and/or right timelike boundaries.

One can see that this patch consists of a Schwarzschild-like hexagon with de Sitter "wings" attached at left and right side. This spacetime still has the Schwarzschild spacelike singularity, but past and future conformal infinities are now spacelike, not null. There are two horizons inherited from the constituents, a Schwarzschild-like event horizon and de Sitter-like particle horizon. An "unwrapped" SdS space consisting of infinitely many such patches was described by Gibbons and Hawking in [10]. The subset of a full SdS spacetime we are concerned with is much smaller. Since we are interested in observing radiation from the vicinity of a black hole, we include only the parts that are in the causal past and the causal future of the black hole, as shown on figure 2.2. This spacetime is well described by the metric (2.1). We are only interested in the static region between the event horizon and the particle horizon.

In our calculations, we consider null geodesics extended toward the black hole accretion disk, instead of collecting null geodesics emanating from it. This corresponds to time reversal, which is a global symmetry of any static spacetime.

The rombus-shaped static region of the SdS spacetime is bounded by the two horizons and is the area where a timelike observer can remain forever. This region exists only if the cosmological constant Λ is not too large relative to the black hole mass, such that there is a region where $T(r) > 0$. If this condition is violated, then the SdS spacetime has no

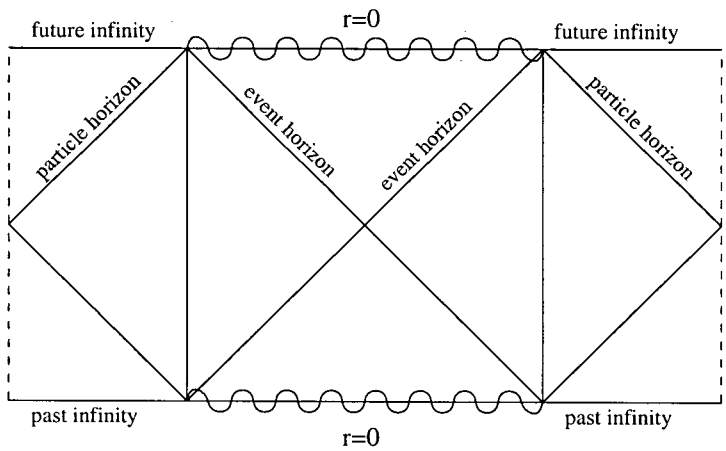

Figure 2.1: The Penrose-Carter diagram of an SdS spacetime patch.

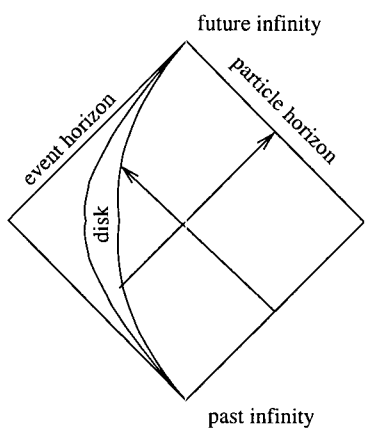

Figure 2.2: The Penrose-Carter diagram of a static patch of an SdS spacetime containing causal past and future of an accretion disk around the central black hole.

horizons and contains a naked singularity. This can be seen as follows: for large Λ the term $(1 - \frac{2M}{r} - \frac{1}{3}\Lambda r^2)$ is negative for all r, thus making the t coordinate spacelike everywhere. The function $T(r) = (1 - \frac{2M}{r} - \frac{1}{3}\Lambda r^2)$ has a maximum at $(\frac{3M}{\Lambda})^{\frac{1}{3}}$, and the value of the function at this point is $1-(9M^2\Lambda)^{\frac{1}{3}}$, which is negative for $\Lambda > \frac{1}{9M^2}$. See [23] for a detailed analysis of both Schwarzschild-de Sitter and Schwarzschild-anti-de Sitter spacetimes. Since the motivation for our work is to study accretion disk spectra from cosmological black holes, we will only consider the case where $9\Lambda >> \frac{1}{9M^2}$.

We can now proceed to derive the relevant expressions for line profile calculation. The effective potential for the SdS metric is

$$V_{eff} = \frac{l^2}{2r^2} - \frac{M}{r} - \frac{Ml^2}{r^3} - \frac{1}{6}\Lambda r^2 \tag{2.2}$$

where l is the conserved orbital angular momentum.

Circular orbits correspond to the extrema of this effective potential V_{eff}:

$$\frac{M}{r^2} - \frac{\Lambda r^2}{3} - \frac{l^2}{r^3} + \frac{3Ml^2}{r^4} = 0 \ . \tag{2.3}$$

The circular orbit is stable when the extremum is a minimum:

$$\frac{\Lambda}{3}(4 - \frac{15M}{r}) < \frac{M}{r^3}(1 - \frac{6M}{r}) \ . \tag{2.4}$$

For $\Lambda M^2 = 0$, we recover the familiar circular orbit stability limit for the Schwarzschild metric: $r > 6M$ [18]. We now examine in more detail the orbit stability for the case where the spacetime is close to that of Schwarzschild, namely that of small cosmological constant relative to the black hole mass, $2M << \sqrt{\Lambda/3}$ and distances far from the black hole, $d >> 2M$.

For small enough ΛM^2, the minimum stable circular orbit is approximately $r_{min} \simeq 6M + 648\Lambda M^3$. Unlike the case of the Schwarzschild solution, circular orbits become unstable at both small and large radius in the metric: the "negative pressure" produced by the cosmological constant destabilizes the outer circular orbits. This effect will limit the value of Λ for which the Schwarzschild-de Sitter metric makes sense as a background for a black hole with an accretion disk. From (2.4) we can calculate that the maximum possible stable orbit is approximately at

$$r_{max} = (\frac{3M}{4\Lambda})^{\frac{1}{3}} \tag{2.5}$$

Objects beyond this limit would either find a smaller stable circular orbit or become unbound. See [23, 24] for an exhaustive discussion of timelike and null geodesics in the SdS spacetime. For black holes of between 1 and 10^{10} solar masses, a range from stellar remnant black holes to the mass of active galactic nuclei, the current estimated value of Λ yields an r_{max} of the order of 20 to 40,000 parsec.

The linear rotational velocity seen by the observer of an element of the disk at radius r is

$$v = \sqrt{\frac{M}{r} - \frac{\Lambda r^2}{3}}, \tag{2.6}$$

or slower than the velocity at the same radius in the Schwarzschild metric, $v = \sqrt{\frac{M}{r}}$. This is as expected, as the cosmological term acts as a repulsive force and partially screens the central mass [1].

To make the overall frequency shift in the spectrum unambiguous, we need to choose an observer. We will assume that the observer has zero radial velocity relative to the black hole; with this assumption, the observer's 4-velocity coincides with (1.8) and g_{obs} becomes

$$g_{obs} = \frac{1}{\sqrt{1 - \frac{2M}{d} - \frac{\Lambda}{3}d^2}}. \tag{2.7}$$

. The contribution from the disk is

$$g_{disk} = \frac{\sqrt{1 - \frac{3M}{r}}}{1 - \frac{b}{r}\sqrt{\frac{M}{r} - \frac{1}{3}\Lambda r^2}\sin\alpha} . \tag{2.8}$$

As discussed in chapter 1, g_{obs} is independent of the integration parameters in (1.16) and can be factored out of the integral; (1.16) becomes

$$F_\nu = \frac{\kappa g_{obs}^3}{4\pi d^2}\int g_{disk}^3 \frac{r\sin\theta}{b\cos i} r^{-p}\delta(\nu - g\nu_0) b db d\phi . \tag{2.9}$$

The factor $\frac{\kappa g_{obs}^3}{4\pi d^2}$ depends on both the distance to the accretion disk d and Λ; the integrand is now independent of d.

2.2 Results for Schwarzschild - de Sitter Metric

The line profile in the Schwarzschild-de Sitter metric is similar to that of the Schwarzschild case; however the normalized line profile now depends on four dimensionless parameters. The additional parameter is ΛM^2 as discussed in section 2.1. In addition, note that the absolute position of the blue peak in frequency will in principle depend on both the distance to the observer and the cosmological constant. However, for the range of ΛM^2 in our simulations, this effect is negligible.

Fig. 2.3 shows the effects of cosmological constant on the normalized accretion disk fluorescence spectra for the disk of inner radius $7M$ and outer radius $70M$, fixed disk inclination $i = 30^{\circ}$ and a constant emissivity index $p = 2$. The parameter ΛM^2 is varied from 1×10^{-8} to 2.2×10^{-6}. This maximum value of ΛM^2 corresponds to an maximum outermost stable orbit of radius $70M$ (cf. 2.5). This data set is similar to that in Fig.1 of [8]. However, note that for most of the data sets used in [4, 8], the outer radius exceeds the radius of the outermost stable circular orbit values of $\Lambda M^2 = 10^{-7}$, which is barely large enough to produce a noticeable difference in the spectrum. The simulation shows that the effects are negligible for ΛM^2 below about 10^{-7}. Above that, the relative height of the red peaks get progressively larger with the increase of the cosmological term. In addition, the peaks tend to get closer together.

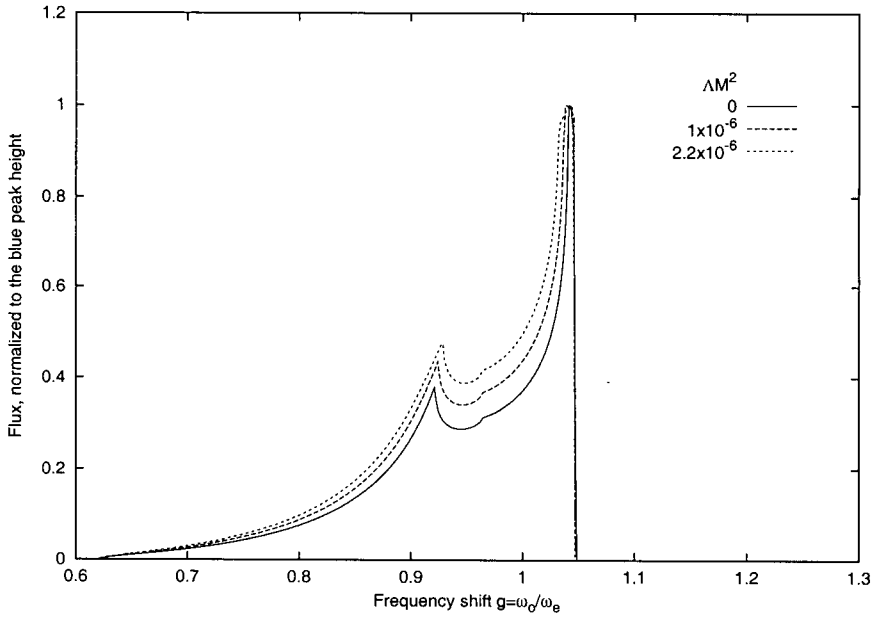

Figure 2.3: Spectra calculated for a range of ΛM^2 for inclination angle $i = 30°$, $p = 2$, $r_{min} = 7M$, $r_{max} = 70M$. Note that the line for $\Lambda M^2 = 1 \times 10^{-7}$ coincides with that for the Schwarzschild case on this graph.

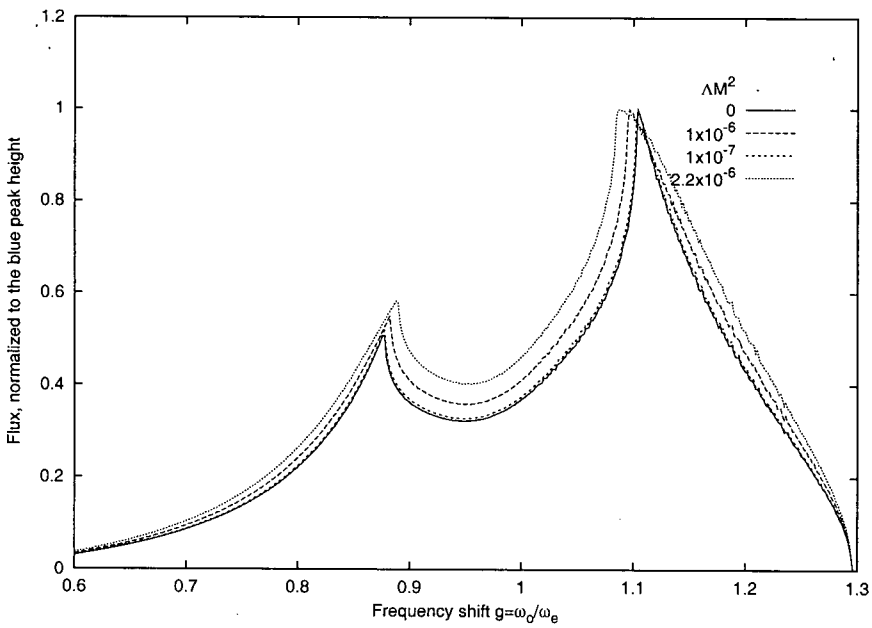

Figure 2.4: Spectra calculated for a range of ΛM^2 for inclination angle $i = 70°$, $p = 2$, $r_{min} = 7M$, $r_{max} = 70M$.

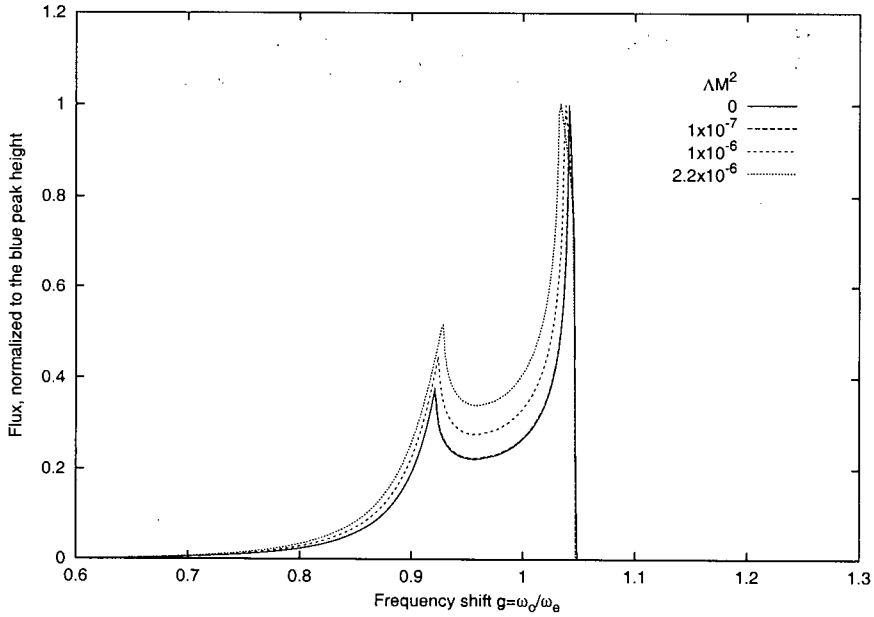

Figure 2.5: Spectra calculated for a range of ΛM^2 for inclination angle $i = 30°$, $p = 1$, $r_{min} = 7M$, $r_{max} = 70M$. Note that the line for $\Lambda M^2 = 1 \times 10^{-7}$ coincides with that for the Schwarzschild case on this graph.

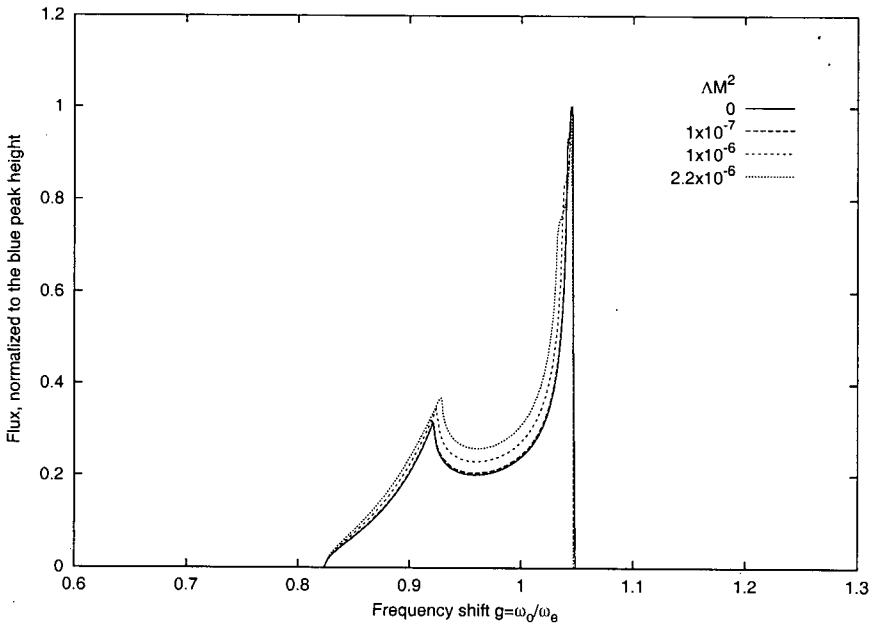

Figure 2.6: Spectra calculated for a range of ΛM^2 for inclination angle $i = 30°$, $p = 2$, $r_{min} = 20M$, $r_{max} = 70M$. Note that the line for $\Lambda M^2 = 1 \times 10^{-7}$ coincides with that for the Schwarzschild case on this graph.

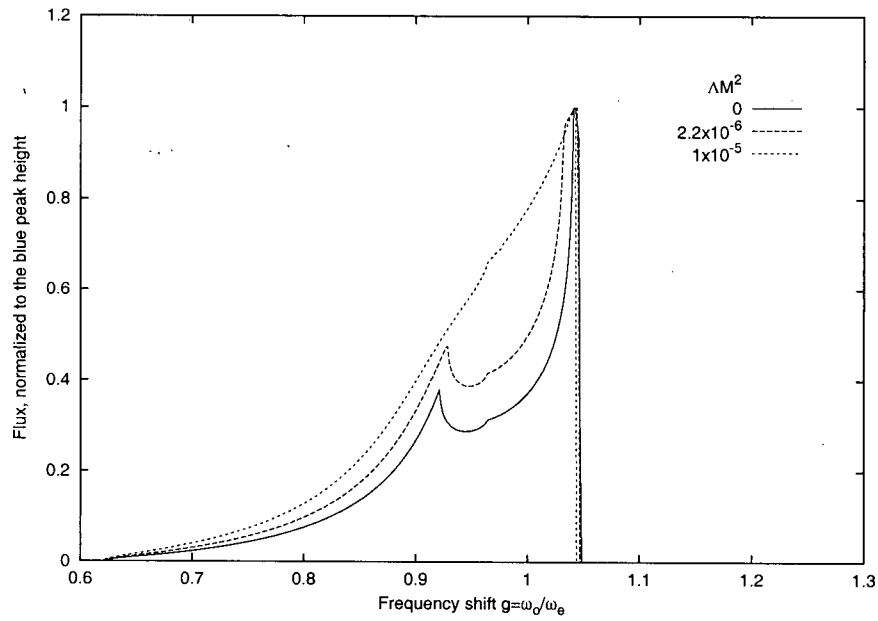

Figure 2.7: Spectra calculated for $\Lambda M^2 = 10^{-5}$ for inclination angle $i = 30°$, $p = 2$, $r_{min} = 7M$, $r_{max} = 70M$ versus the maximum allowed by orbit stability condition, $\Lambda M^2 = 2.2x10^{-6}$.

Figures 2.4-2.6 show the dependence of spectra on the cosmological term for the specified values of inclination angles, emissivity index and disk dimensions. The results are similar to that illustrated in equation (2.6) for all cases.

As discussed earlier, the data above are limited to the parameter sets that ensure stable circular orbits for all parts of the disk. Much more dramatic differences from Schwarzschild spectra can be obtained if the condition of Keplerian orbit stability at the outer disk is neglected. Consider, for example, a line profile for $\Lambda = 10^{-5}$ and $p = 2$ (see Fig. 2.7).

2.3 Discussion

One can intuitively understand the effects of the cosmological constant as follows: Λ acts as a negative pressure, reducing the rotational velocity of the disk at a given radius in comparison to the Schwarzschild case. The farther away a circular geodesic is from the black hole, the more pronounced is the velocity reduction. Now most of the material is concentrated in the outer layers of the disk and as the red (blue) peak is produced by the parts of the disk moving fastest away (towards) the observer, slower rotational velocity farther away means less pronounced peaks. This effect is somewhat similar to that of

[1]At $r = (\frac{3M}{\Lambda})^{\frac{1}{3}}$ the central mass is completely screened, so that a particle can "hover" at that distance without rotating at all. This distance, however, is farther from the center than the maximum stable circular orbit, and so the equilibrium is unstable.

reducing the maximum outer radius or increasing the emissivity index, both of which shift the relative contribution to the spectrum in favor of the inner parts of the disk.

One can estimate the magnitude of the cosmological constant required to see its effect on the accretion disk line shape for black holes of 10^6 to 10^8 solar masses. Assuming the cosmological constant value consistent with the current observations, $\Lambda = \Omega_\Lambda h^2 = 0.33 \pm 0.05$, calculated from the WMAP-based values for the dark matter density $\Omega_\Lambda = 0.68 \pm 0.03$ (Ω_c is set to 1), the Hubble constant $h = 0.72 \pm 0.04100 km/s/Mpc$ ([14]), and a black hole of 10^8 solar masses, we get the factor $\Lambda M^2 = 1.2 \cdot 10^{-27}$. To produce a noticeable effect on the accretion disk spectrum this factor has to be at least as large as 10^{-7}, which requires either an increase in Λ by 20 orders of magnitude or an increase in a black hole mass by 10 orders of magnitude to 10^{18} solar masses. Thus observations of the line shape of the iron line profile do not provide sensitive independent bounds on the cosmological constant.

Chapter 3

Einstein-Yang-Mills Line Profiles

Einstein-Yang-Mills (EYM) solutions are the solutions of Einstein equation coupled to the Yang-Mills fields. The interest in the EYM solutions was sparked by the paper of Bartnik and McKinnon in which they numerically constructed a family of static spherically-symmetric EYM spacetimes that are regular everywhere ([2]). Soon afterwards the existence of such spacetimes was proved analytically by Yau and coworkers ([22]). Besides regular solutions, there are also black-hole ones, i.e those that have a singularity inside a horizon. It is not inconceivable that Yang-Mills field may have played a role in formation of primordial black holes originally proposed by Hawking in [11].

In the following we only consider gravity coupled to the Yang-Mills fields with SU(2) gauge group. For a generic SU(N) Yang-Mills gauge field the character of solutions is qualitatively the same. See [26] for review and [13] for an example of magnetically-charged solutions. We did not investigate the accretion disk spectra from such solutions. Finding them is more difficult, as one has to deal with increasing number of parameters, and chances are, in the area where accretion disks may exist, there won't be any significant differences from the SU(2) EYM solutions.

It has been shown that EYM equations with static spherically-symmetric ansatz admit several types of solutions. Since our goal is to obtain accretion disk line profiles seen by a remote observer unaffected by the local effects, we only consider asymptotically flat (AF) solutions. A generic EYM solution is not asymptotically flat and so one has to fine-tune the parameters to satisfy the AF boundary conditions. The stability of asymptotically flat EYM solutions has been studied extensively, both numerically and analytically (see [26] and references therein). All static spherically symmetric solutions have been found perturbatively unstable with the time scale of the order of 20 times their characteristic size (see e.g. [16]) Still, they might occur during evolution of other, dynamic, solutions. One should also note that there are stable regular and black hole solutions for Yang-Mills-Higgs fields (see references in [26]), and we may expect the accretion disk line profile features to be qualitatively similar.

Section 3.1 outlines the EYM equations and the general properties of their AF solutions. Unlike the Schwarzschild and Schwarzschild-de Sitter case metrics, the EYM metrics are not known analytically, so they have to be computed numerically before we can calculate the accretion disk spectra. Section 3.2 discusses different approaches to finding these solutions numerically. Section 3.3 lists our results for the numerically obtained regular and black-hole metrics and compares them with literature. Once the metric is known, we can proceed with calculating circular orbits and null geodesics in order to get the line profile. As in the Schwarzschild - de Sitter case, one has to carefully analyze the circular orbit stability first. Section 3.4 analyzes the circular timelike orbit stability in EYM metrics. Finally. section

3.5 presents our computed line profiles and discusses their features.

3.1 Metric

First we outline how to obtain the equations for the metric of static spherically symmetric solutions of the Einstein-Yang-Mills theory. Here we follow the review by Volkov and Gal'tsov [26]. We will start from the action and obtain first the general field equations and then simplify them using the symmetries of the spacetime.

The action of this theory is

$$S_{\mathrm{EYM}} = \int \left\{ -\frac{1}{16\pi G} R - \frac{1}{8g^2} \operatorname{tr} F_{\mu\nu} F^{\mu\nu} \right\} \sqrt{-det\{g_{\mu\nu}\}}\, d^4x \,, \tag{3.1}$$

where G is the gravitational constant, g is the gauge coupling constant. $F_{\mu\nu}$ is the Yang-Mills (YM) field strength

$$F_{\mu\nu} = \partial_\mu A_\nu - \partial_\nu A_\mu - i[A_\mu, A_\nu] \;\equiv\; \frac{1}{2}\tau_a F^a_{\mu\nu} \tag{3.2}$$

traced over the Lie algebra index and

$$A \equiv A_\mu dx^\mu \equiv \frac{1}{2}\tau_a A^a_\mu dx^\mu \tag{3.3}$$

is the YM SU(2)-valued gauge field, where τ_a is the basis of the SU(2) algebra. The variation of the action with respect to the metric gives the Einstein equations

$$R_{\mu\nu} - \frac{1}{2} R\, g_{\mu\nu} = 8\pi G\, T_{\mu\nu} \tag{3.4}$$

with the Yang-Mills stress-energy tensor

$$T_{\mu\nu} = \frac{1}{2g^2} \operatorname{tr} \left(-F_{\mu\sigma} F_\nu{}^\sigma + \frac{1}{4} g_{\mu\nu}\, F_{\alpha\beta} F^{\alpha\beta} \right). \tag{3.5}$$

The variation with respect to the Yang-Mills field gives the field equations

$$D_\mu F^{\mu\nu} \equiv \nabla_\mu F^{\mu\nu} - i[A_\mu, F^{\mu\nu}] = 0. \tag{3.6}$$

Similarly to electromagnetism, one can show that the dual field tensor $*F_{\mu\nu} \equiv (1/2)\sqrt{-g}\, \epsilon_{\mu\nu\rho\sigma} F^{\rho\sigma}$ satisfies the Bianchi identities

$$D_\mu *F^{\mu\nu} \equiv 0\,. \tag{3.7}$$

We now need to simplify these equations assuming the solution is static and spherically symmetric. This spacetime symmetry is the rotation group of spatial rotations SO(3) and the time translation. These restrict the metric to the form 1.3:

$$ds^2 = -T(r)dt^2 + R(r)^{-1}dr^2 + r^2 d\Omega^2. \tag{3.8}$$

In the purely magnetic YM gauge choice the form of the field then becomes

$$A = w\tau_2 d\theta + (\cos\theta\tau_3 - w\tau_1 \sin\theta)d\phi, \tag{3.9}$$

(see e.g. [3] and references therein). Thus we have a single real function $w(r)$ representing the YM gauge field and two real functions $T(r)$ and $R(r)$ representing the radial and temporal metric components. The equations 3.4 - 3.7 reduce to a system of ODEs. For convenience, we first rewrite the metric functions as

$$\begin{aligned} T(r) &= A(r)C(r)^2 \\ R(r) &= A(r). \end{aligned} \tag{3.10}$$

Now $A(r)$ and $C(r)$ obey the equations

$$\begin{aligned} rA' + 2Aw'^2 &= \frac{\Phi}{r} \\ r^2 Aw" + \Phi\, w' + uw &= 0 \\ rC' &= 2Cw'^2, \end{aligned} \tag{3.11}$$

where u and Φ are simple functions of r, A and w:

$$\begin{aligned} u &= 1 - w^2 \\ \Phi &= r(1-A) - \frac{u^2}{r}. \end{aligned} \tag{3.12}$$

Here we have rescaled the radial variable $r \to \frac{r\sqrt{G}}{g}$ to remove the dependence on the coupling constants G and g. In the rest of this chapter we'll use horizon radius $r_h = 1$, which defines the actual horizon radius unambiguously, provided the strength of SU(2) coupling g is fixed. However, since the action 3.1 admits rescaling $r \to \frac{r}{\lambda}$, $F(r) \to \lambda\, F(\frac{r}{\lambda})$, any solution can be scaled to a desired size or mass by changing the ratio of the coupling constants $\frac{G}{g^2}$.

We will often compare the EYM solutions with the Schwarzschild and the extreme Reissner-Nordstrom, where $Q = M$. Here, for completeness, are the metric functions of the last two, expressed in the usual Schwarzschild coordinates, with a single parameter r_h, the horizon radius (also the location of the singularity in the extreme Reissner-Nordstrom metric):

$$T(r) = R(r) = 1 - \frac{r_h}{r} \tag{3.13}$$

(Schwarzschild) and

$$T(r) = R(r) = (1 - \frac{r_h}{r})^2 \tag{3.14}$$

(Reissner-Nordstrom).

For asymptotic flatness the metric functions should approach constant finite value at infinity. In the EYM case this means that both $(1 - w^2)$ and $(1 - A)$ must go to zero (see

[20] for details). Thus, we can use asymptotic expansions near $r = \infty$:

$$|w| = 1 - \frac{a}{r} + O(r^{-2})$$
$$A = 1 - \frac{2M}{r} + O(r^{-2}) \tag{3.15}$$

Here a and M are constant parameters. M is ADM mass. $C(r)$ will automatically stay finite at infinity and can be rescaled to $C(\infty) = 1$.

Unlike Abelian gauge fields, such as electromagnetism, non-Abelian gauge fields coupled to gravity admit static spherically-symmetric solutions that are regular everywhere, including at $r = 0$. These solutions were first numerically discovered by Bartnik and McKinnon for SU(2) Einstein-Yang-Mills case ([2]), analytically shown to exist in [22], and then expanded to other cases, see [12] for review. In this case $A(r)$ and $w(r)$ stay finite at $r = 0$ and $A(r)$ has no zeros (horizons). We can use the following expansions near $r = 0$:

$$w = 1 - br^2 + O(r^4)$$
$$A = 1 - 4b^2r^2 + O(r^4) \tag{3.16}$$

Here b is a solution parameter, not to be confused with the impact parameter for null geodesics b discussed in chapter 1, as the terminology $b \equiv -\frac{1}{2}\frac{d^2w(0)}{dr^2}$, introduced by Bartnik and McKinnon in their original paper is now standard. To avoid the confusion we will make explicit the meaning of b whenever we use it.

It is easy to check that there are no first-order terms in the expansions (3.16). The condition of regularity together with asymptotic flatness restrict the possible values of the parameters a, M and b to a countable number of possibilities. A standard way to enumerate these solutions is by counting zero-crossings of $w(r)$. This is analogous to counting zeros of the wave function of a bound state in quantum mechanics. Actual solutions will be presented in section 3.3. $n = 0$ is the Schwarzschild spacetime with $w = 1$ everywhere. The first non-trivial solution corresponds to $n = 1$. With increasing n the Bartnik-McKinnon solutions approach the extreme Reissner-Nordstrom for $r >> 1$, with w oscillating wildly near $r = 1$, albeit with a very small amplitude. This convergence has been noted in a number of papers, see e.g. [22].

If we allow $A(r)$ to have nodes, we get a black hole solution. Each node represents an event horizon. For the purpose of studying accretion disk spectra, we, of course, only care about the outermost node, as there is no radiation emitted from inside the outer horizon. The boundary conditions for a given horizon radius r_h are determined, under an assumption of finite curvature and field strength, by a single parameter w_h, the field strength on the horizon (see e.g.[26] equations 4.5, 4.6):

$$w = w_h + \frac{r_h w_h (w_h^2 - 1)}{1 - \frac{(w_h^2-1)^2}{r_h^2}}(r - r_h) + O(r^2)$$
$$A = \frac{1}{r_h}(1 - \frac{(w_h^2 - 1)^2}{r_h^2})(r - r_h) + O(r^2) \tag{3.17}$$

Similarly to the regular case, only discrete values of the parameter w_h lead to asymptotically-flat solutions, which can also be enumerated by counting zero-crossings of w. w_h and the parameters of asymptotic expansion at infinity a, M are completely determined by specifying horizon radius r_h and the solution number n, where n is the number of zero crossings of w. Just as in regular case, the black-hole solutions approach extreme Reissner-Nordstrom for large n ([21]).

The behavior of the SU(2) EYM solutions is characteristic of higher gauge groups, as well. For static spherically-symmetric asymptotically flat SU(N) EYM solutions the gauge field strength has $N-1$ components w_i remaining after gauge fixing (see references in [26], section 4.4). Each such solution can be defined by the horizon radius $r_h = 0$ ($r_h = 0$ for regular case) and $N-1$ integers, corresponding to the number of zeros in each of the $N-1$ components w_i of the gauge field strength.

3.2 Numerical Methods

In this section we outline our approach to numerically finding asymptotically flat solutions of the EYM equations.

To get a good resolution of the metric finctions $A(r)$ and $T(r)$ near the horizon necessary for obtaining accurate line profiles, and at the same time ensure asymptotic flatness, it is convenient to rescale the radial coordinate to emphasize the interesting areas of the disk, using $r \to \ln(r)$. This is discussed in appendix A.3.

To get the metric we need to solve the system (3.11) with the boundary conditions 3.15 and either 3.16 (for Bartnik-McKinnon solutions) or 3.17 (for black-hole solutions). There are several ways to approach this. Bartnik and McKinnon used a simple one-parameter shooting method, where regular boundary conditions at $r = 0$ were matched against $w = 1$ at infinity by varying expansion parameter b in equation (3.16). We do so as well. We now review why this method is chosen.

A simple way to find a black hole solution would be to start with an asymptotic expansion 3.15, arbitrarily choose parameters a and M and use one of the standard integration methods, such as Runge-Kutta to extend the solution toward $r = 0$. This way our solution is guaranteed to be asymptotically flat, and it will have to be either regular or a black hole, as there are no other types. This strategy, however, has a number of problems. Even assuming infinitely accurate calculations, we will only ever get BH solutions, as they form a continuous set, if you let the horizon radius r_h vary. Regular solutions would have to be taken as limits of BH solutions with the very small horizon radius. Also, due to the extreme sensitivity of solutions to the parameter values, it is very hard to sample the parameter space fine enough to obtain all the desired solutions, such as those with interesting horizon radius, fixed number of nodes in w etc. The situation gets much worse if we account for the numerical error inevitably introduced in the calculations. This error dominates when the metric function $A(r)$ becomes small, such as near the expected BH horizon. The result is usually quite dramatic: the metric and field strength functions start growing out of control, indicating catastrophic precision loss. In the end, it is rather difficult to determine the domain of validity of the numerical solution and where the horizon should have been.

Alternatively, one could start with a boundary condition near $r = 0$ or $r = r_h$, sampling the single-parameter space (b for regular solutions, w_h for black hole solutions) and extend the solution numerically towards large r. of course, almost all solutions obtained this way would not be asymptotically-flat even if there were no numerical error. Given this error, even a numerical solution with the best guess of the parameter would only track the "true" solution to a finite r before diverging exponentially. Again, it would be really hard to find a solution with a desired number of nodes in w without knowing it in advance, but at least the accuracy of the solution in the crucial area near $r = r_h$ or $r = 0$ is guaranteed to be good.

The standard way to approach problems like that is to use a shooting method with fixed point matching. See the classic reference [19], chapter 17 for excruciatingly detailed discussion and code samples. In a nutshell, we fix both the inner and outer boundary as desired and then sample the parameter space (either (a, M, b) or (a, M, w_h)) trying to find solutions that converge to the same values somewhere inside the domain of integration. This brings the problem into the domain of finding a minimum of a function of several variables, where the function is some estimate of the mismatch between the inward and outward solutions and the variables are the solution parameters. There are readily available methods to solve this problem, most notably the Newton-Raphson method for multi-dimensional minimization and Brent method for one-dimensional minimization. Of course, one still needs a good initial guess to get a particular solution, as there are many local minima in the parameter space. If the initial guess isn't good, the method may either not converge at all, or find a solution with a radically different set of parameters. But at least the sampling of the parameter space is automatic and usually rather efficient. For our calculations we mainly use the routines from [19], occasionally with some minor modifications to fine-tune the precision and the discretization of the metric.

We successfully implemented both approaches, and the resulting metrics coincide with a very good accuracy. For a one-dimensional minimization we used Brent method with the parameter b from (3.16) for the regular solution, and with the parameter w from (3.17) for the black-hole solution. Choosing a good function to minimize was one of the interesting problems. The domain of integration for the routine *odeint* from [19] has to be set in advance. In our case we fixed it at $r = 10^9$, which is large enough for all parameter values. However, the numerical solution usually stops tracking the asymptotically flat one before the end of the domain of integration is reached and then diverges very quickly once $|w|$ exceeds unity for the first time. We thus stop the integration as soon as the condition $|w| < 1$ is triggered, without waiting for the solution to diverge. Since we want our solution to be as close to the asymptotically flat as possible, we use negative of the divergence distance as our minimization function.

A way to look at the AF solution tracking breakdown is to think of the numerical solution obtained as a real non-AF solution, with a singularity at a certain radius r_s. As the parameter approaches some critical value where the solution is asymptotically-flat, r_s goes to infinity. One would expect a scaling law similar to that of a phase transition:

$$r_s = C(p - p^{AF})^{\gamma}, \tag{3.18}$$

where p is the parameter such as b or w_h. p^{AF} is the value of this parameter for an AF

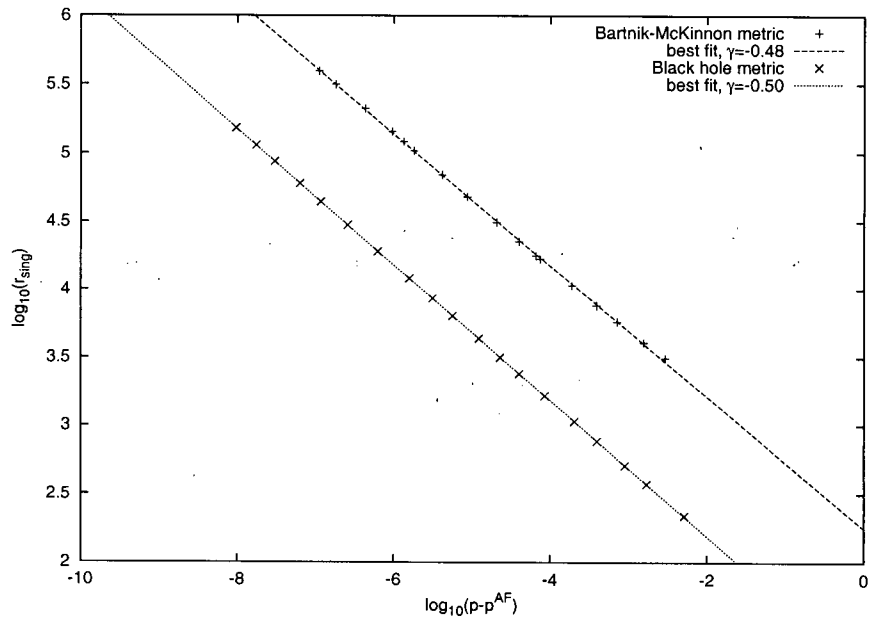

Figure 3.1: Distance to the singularity as a function of $p - p^{AF}$, where p is the fitting parameter (w_h or b, depending on the metric) p^{AF} is the value of this parameter for the asymptotically flat solution.

solution, and γ is the scaling exponent. Figure 3.1 shows the scaling law for two such examples, one for a regular Bartnik-McKinnon solution with $n = 1$, and another for a black hole solution with horizon radius $r_h = 1$ and $n = 1$. The critical exponent in one case is $-.48$ and in the other case -0.50. This may be related to the scaling behavior numerically found in [3] for the divergence radius of a generic solution: $r \propto |b|^{-\frac{1}{2}}$. The figure 3.1 only shows the region where the power law holds well. In reality, the slope of the lines levels off for small $|p - p^{AF}|$ due to numerical errors. Assuming that in the ideal case the scaling should hold to arbitrary precision, we can use the point where the scaling breaks down, p_{best} to estimate the accuracy of p_{AF}:

$$p^{AF} = p^* \pm |p_{best} - p^*|, \tag{3.19}$$

where p^* is the parameter value found by the minimization routine. We are not aware of this approach to evaluating the solution accuracy having being applied before.

Yet another approach to get the metric numerically would be to use relaxation methods, either instead of, or in addition to the shooting methods. In the relaxation method, the initial "guess" solution is specified, which is then iteratively relaxed to the "true" solution. An advantage of relaxation methods is that we could start with a trial solution that has a given structure, such as the number of nodes in w, and hope that this structure is preserved during relaxation process. A good initial guess can be found by first using a shooting method. See chapter 17.3 of [19] for details. We did not try to implement this approach,

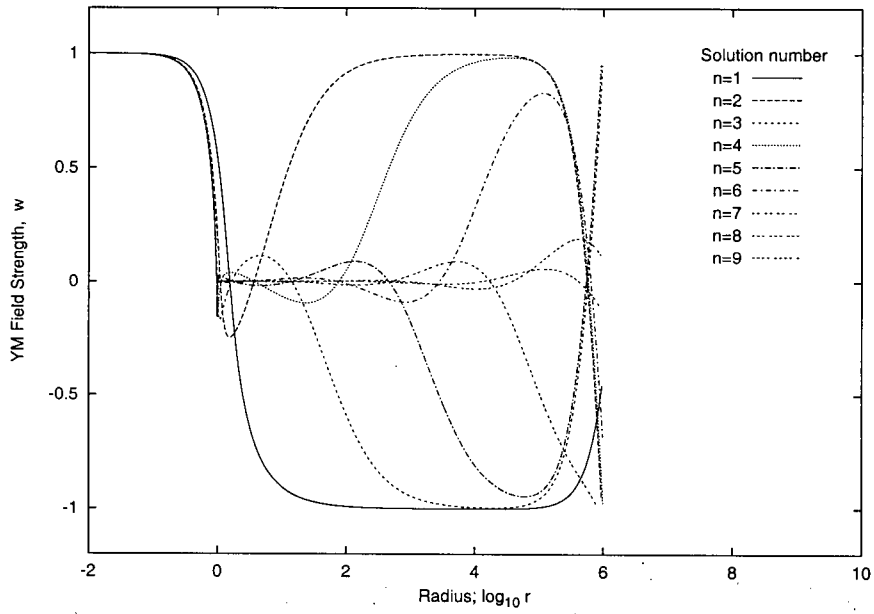

Figure 3.2: First 7 Bartnik-McKinnon solutions. Only the YM field strength w is shown. Solutions are enumerated by the number of nodes of w. Note the tracking breakdown at large r.

however, as one-dimensional minimizations and shooting to a fixed point provided adequate performance.

A note about the metric function $C(r)$. Since it is defined only up to a constant factor, we are free to choose any value of C at any one point, so we choose the standard convention of $T(\infty) = 1$, which implies $C(\infty) = 1$.

3.3 Numerical Solutions

Figure 3.2 and table 3.3 show first 7 Bartnik-McKinnon solutions; figure 3.3 and table 3.3 show first 5 black hole solutions. Note that all numerical solutions stop tracking and diverge near $r = 10^5$.

Note on the parameter accuracy. Most papers give only 4 significant figures for the tuning parameter b, likely because the computed value of the parameter depends slightly on the numerical scheme used and even on the initial guess, and the deviations start in the 5th to 7th significant digit. Comparison with the data from [3] shows that the computed values of b match to 5 to 10 significant digits, depending on the node number.

The table 3.3 shows the parameter values for the EYM black hole metric. For the black-hole EYM metric we compared the one-dimensional minimization method which gives us w_h with multi-dimensional Newton-Raphson minimization (routines *newt* and *shootf* from [19]). This gave us the parameters w_h, M, a for the black-hole EYM metric. The rationale

Table 3.1: Parameters of the first 7 Bartnik-McKinnon solutions obtained by shooting to an AF solution

n	b_n	$C_n(0)$
1	0.45371	0.3956
2	0.65172	0.0238
3	0.69704	0.0083
4	0.70487	0.0018
5	0.70617	$3.5 \cdot 10{-}4$
6	0.70640	$1.6 \cdot 10{-}5$
7	0.70641	$7.7 \cdot 10{-}5$

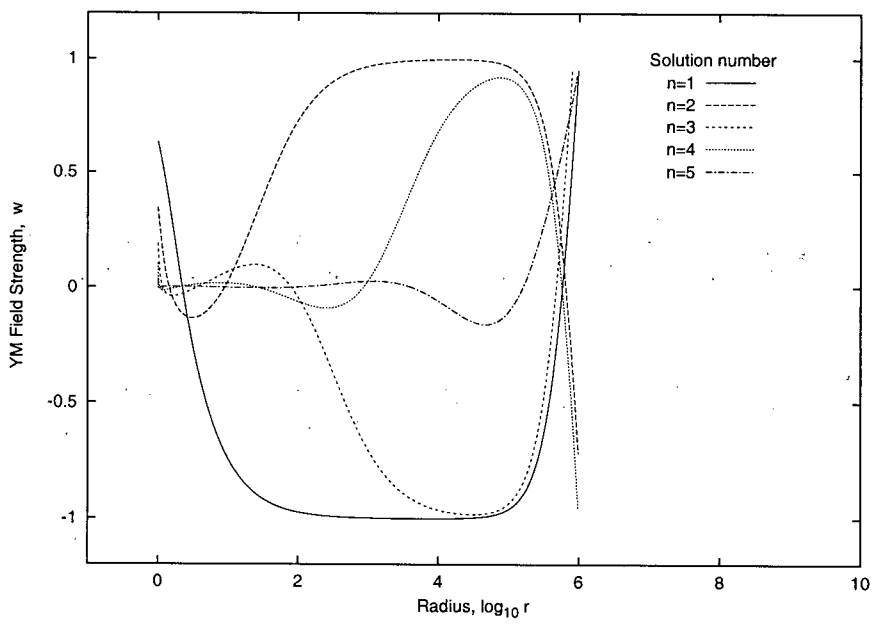

Figure 3.3: First 4 Black hole solutions. Only the YM field strength w is shown. Solutions are enumerated by the number of nodes of w. Note the tracking breakdown at large r.

Table 3.2: Parameters of the first 5 $r_h = 1$ black-hole solutions.

n	w_n	$C_n(0)$	$1 - M_n$	a_n
1	0.6322068	0.39	$6 \cdot 10^{-2}$	2.7
2	0.3551781	0.49	$5 \cdot 10^{-3}$	31
3	0.1875794	0.52	$8 \cdot 10^{-4}$	$5.0 \cdot 10^2$
4	0.1022291	0.55	$5 \cdot 10^{-5}$	$4.2 \cdot 10^3$
5	0.0345178	0.62	$1 \cdot 10^{-5}$	$1.0 \cdot 10^5$

Table 3.3: Parameters of the $n = 1$ black-hole solutions with different r_h

rh	n	wh	M	a	$2M/r_h$
0.1	1	0.99562	0.83524	0.954477	16.7048
1	1	0.633427	0.937259	2.69928	1.874518
2	1	0.341754	1.2368	9.92055	1.2368
5	1	0.277929	2.59574	31.0453	1.038296
10	1	0.270353	5.04793	63.996	1.009586

for using the multi-dimensional minimization was that it produces the value of M directly, which can then be compared with literature. For the one-dimensional minimization, M has to be calculated from the metric indirectly, by matching it to the asymptotic expansions 3.15, which can be difficult given the solution tracking breakdown at large r. However, we found that one-dimensional minimization converged more reliably and produced more consistent values of w_h when varying the initial conditions. This can be understood as follows. There is in reality only one independent parameter for each solution (such as w_h). Using three parameters for optimization instead of one effectively leads to overspecifying the problem. This in turn produces a well-known effect of the minimized function developing long, narrow and twisted valleys in the parameter space, with the valley floor being almost level, and so the minimization process can conceivably terminate at different points in the parameter space, depending on the initial conditions.

The numerical solutions we obtained for Bartnik-McKinnon and black hole with $r_h = 1$ cases match those found in the literature ([2, 26]), for as long as the numerical solution tracking is good.

The ratio of the ADM mass M from the expansion (3.15) to twice the horizon radius is a good measure of the Yang-Mills field contribution to the solution mass. Table 3.3 lists the parameters of the $n = 1$ solutions for different r_h. One can see that the factor $\frac{2M}{r_h}$, very large for small r_h, drops nearly to 1 with increase in r_h.

3.4 Accretion Disk Structure

Since we've been assuming that accretion disks are made of particles traveling along stable circular timelike geodesics, the next logical step after calculating the metric is to investigate such orbits and their stability. Before we do that, let's recall the circular orbit stability results for other well-known metrics:

1. Schwarzschild: no limits on outer radius, inner radius of marginal stability, $r_{ms} = 6M$
2. Extreme Reissner-Nordstrom: $T(r) = (1 - \frac{M}{r})^2$. There is no limit on the outer disk radius, inner radius is $r_{ms} = 4M$
3. Maximally-rotating Kerr: no outer limit, inner limit $r_{ms} = 1.2M$
4. Schwarzschild-de Sitter: inner limit near for small Λ is that of Schwarzschild, $r_{ms} = 6M$, outer limit at $(\frac{3\Lambda}{4M})^{\frac{1}{3}}$.

For the EYM metrics, the stability of the circular orbits can only be evaluated numerically using the expression A.15 derived in Appendix A.1, where again $T(r) = A(r)C(r)^2$. Since for large enough r the metric approaches Schwarzschild or extreme Reissner-Nordstrom, there is no outer limit on the accretion disk radius. However, the inner orbits are more interesting, especially when the size of the black hole gets progressively smaller.

Figures 3.4 and 3.7 show the metric function $T(r)$ for the regular and the black-hole solutions with $r_h = 1$ respectively. One can see that the first 7 solutions are quite different, but starting at $n = 8$ they approximates extreme Reissner-Nordstrom very closely. Figures 3.6 3.8 show the metric function $R(r)$ for the regular and the black hole solutions with $r_h = 1$. These converge to the extreme Reissner-Nordstrom much faster, with $n = 4$ solution already barely distinguishable. Figure 3.5 emphasizes the features of the metric at small r by plotting the metric in log scale.

It is progressively more difficult to find the black-hole solutions using the expansion (3.17) when the horizon radius r_h gets smaller. This is because of the following reasons. The fitting parameter w_h is the value of the field strength $w(r)$ at the horizon. The EYM BH metric converges to the Bartnik-McKinnon metric in the limit $r \to 0$. But for the Bartnik-McKinnon metric $w(0) = 1$ for all solutions. Thus, the difference in w_h between different BH solutions becomes progressively smaller, and it get more difficult to "convince" the numerical procedure to stop and look for a narrow notch representing a particular solution. One could improve the situation by increasing the expansion near horizon to include next order terms, but then the solution obtained would simply be Bartnik-McKinnon, with $w_h = 1$ and the additional parameter being very close to b of the regular solution. Another, better, way to expand the useful parameter range is to use $A'(r_h)$ instead of $w(r_h)$ as a fitting parameter. We did not attempt to pursue this approach, as we obtained first five solutions for $r_h = 0.1$ with the usual technique, and the solutions are already so close to the Bartnik-McKinnon that it is unlikely that higher n will produce any surprise.

Figures 3.9, 3.10 3.11 show the field strength and the metric functions for the black hole solution with $r_h = 0.1$, and figure 3.12 shows the comparison between the Bartnik-McKinnon solution and the EYM black hole with $r_h = 0.1$.

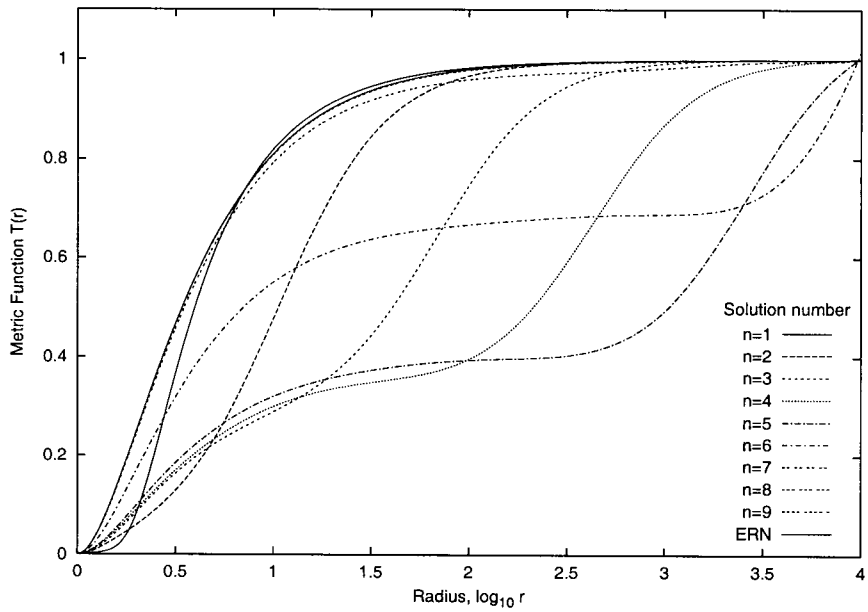

Figure 3.4: The metric function $T(r)$ for the first 9 Bartnik-McKinnon solutions.

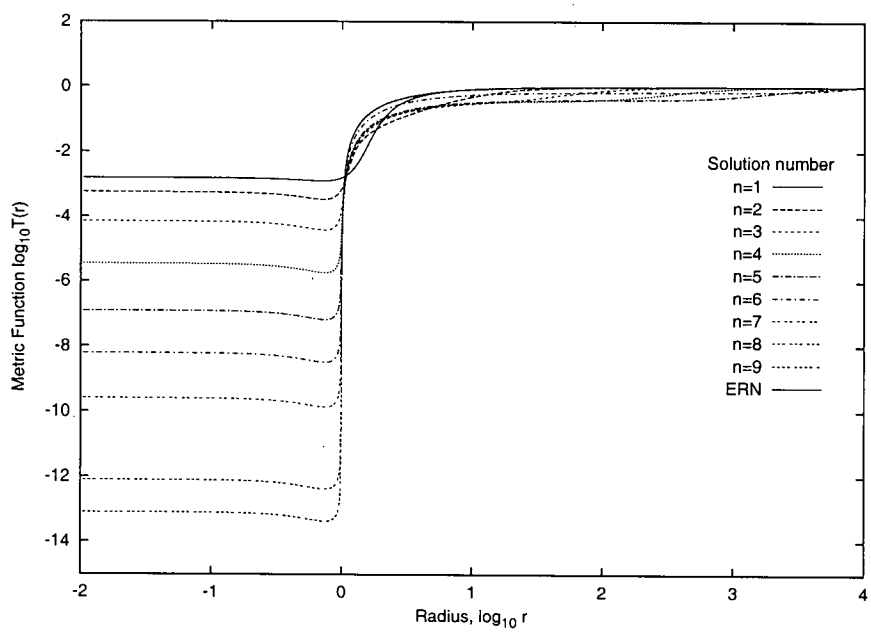

Figure 3.5: The metric function $T(r)$ of the first 9 Bartnik-McKinnon solutions in log scale.

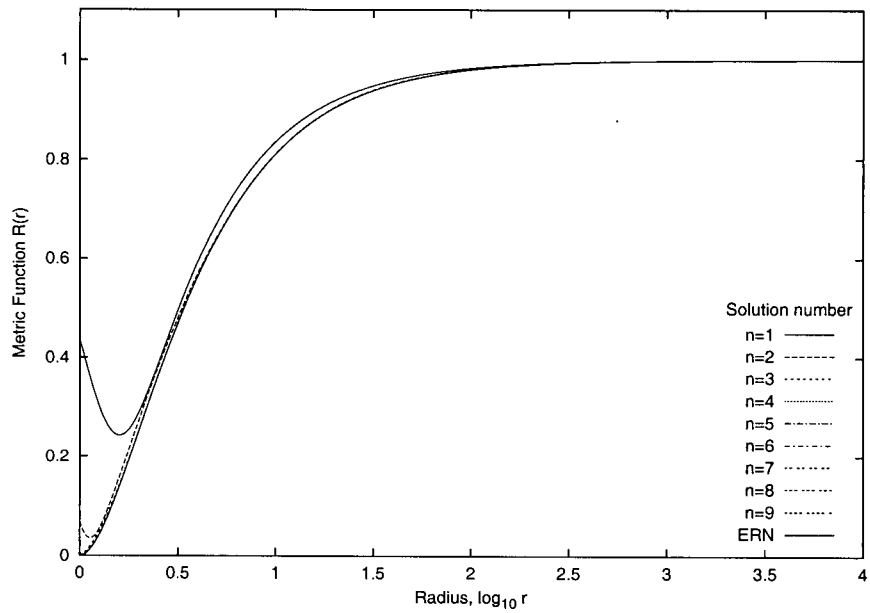

Figure 3.6: The metric function $R(r)$ for the first 9 Bartnik-McKinnon solutions.

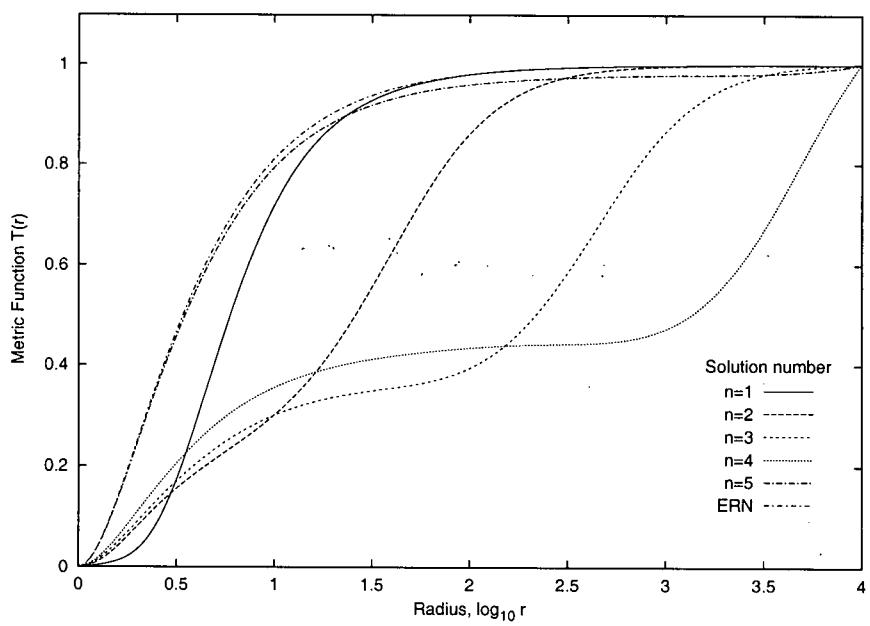

Figure 3.7: The metric function $T(r)$ of the first 5 black-hole solutions with $r_h = 1$, as well as the Schwarzschild and the ERN solutions. The $n = 4$ solution already closely approximates ERN for large r.

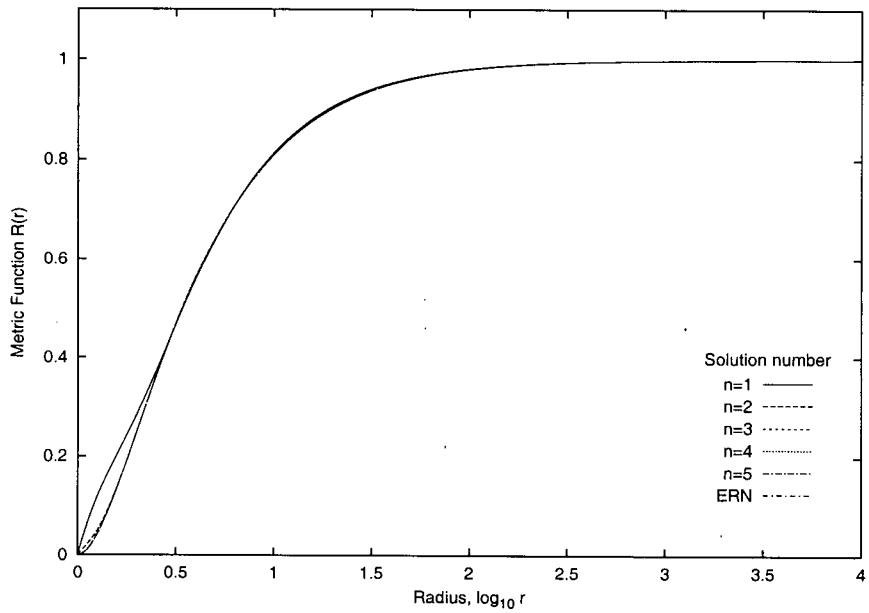

Figure 3.8: The metric function $R(r)$ for the first 5 black-hole solutions with $r_h = 1$, as well as the Schwarzschild and the ERN solutions. The $n = 2$ solution already closely approximates ERN for large r.

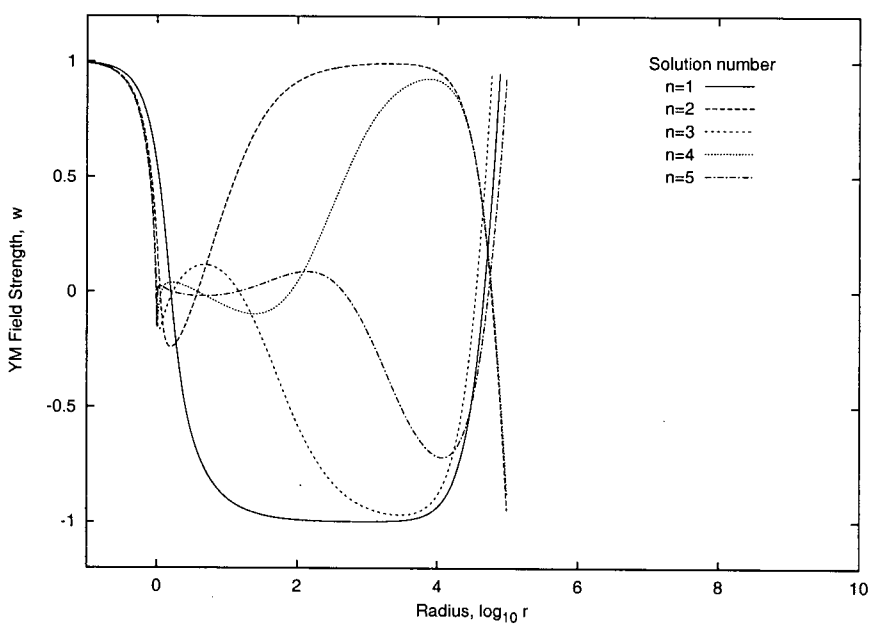

Figure 3.9: The field strength function $w(r)$ for the first 3 black-hole solutions with $r_h = 0.1$.

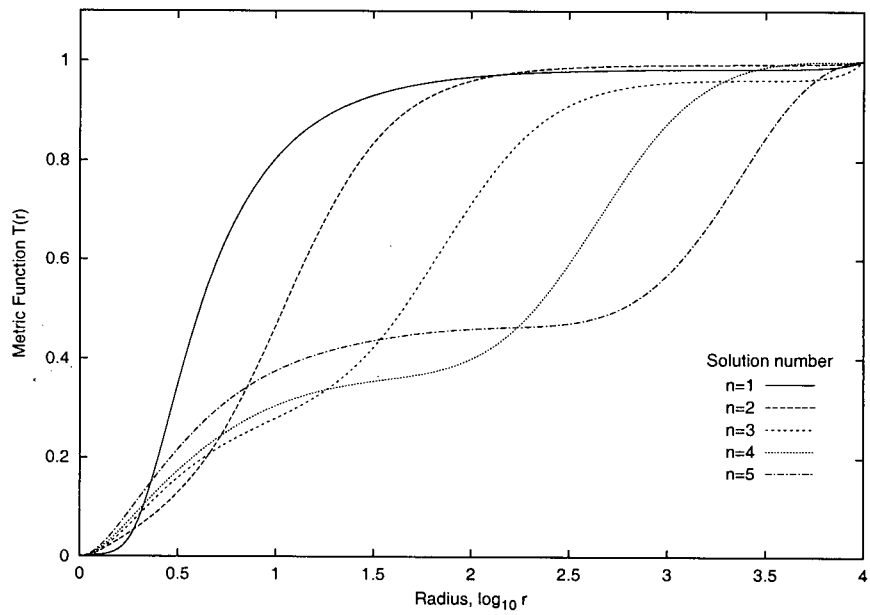

Figure 3.10: The metric function $T(r)$ of the first 5 black-hole solutions with $r_h = 0.1$.

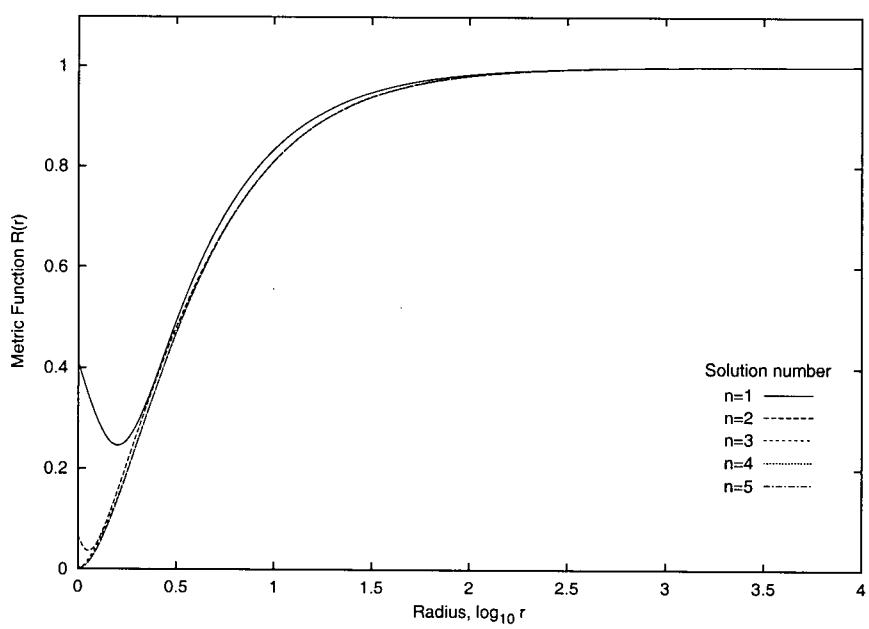

Figure 3.11: The metric function $R(r)$ for the first 5 black-hole solutions with $r_h = 0.1$.

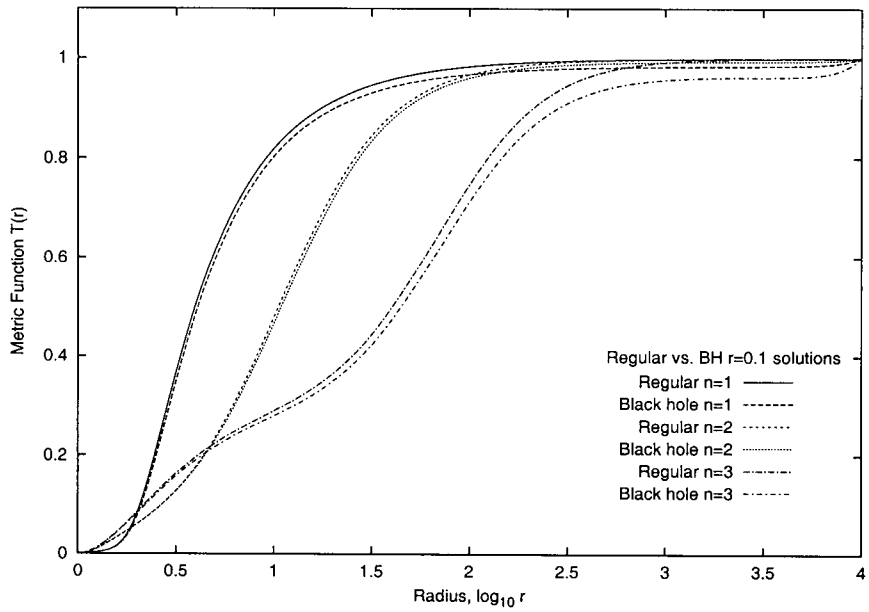

Figure 3.12: Comparison between first 3 Bartnik-McKinnon and $r_h = 0.1$ black hole solutions. Only the metric function $T(r)$ is shown.

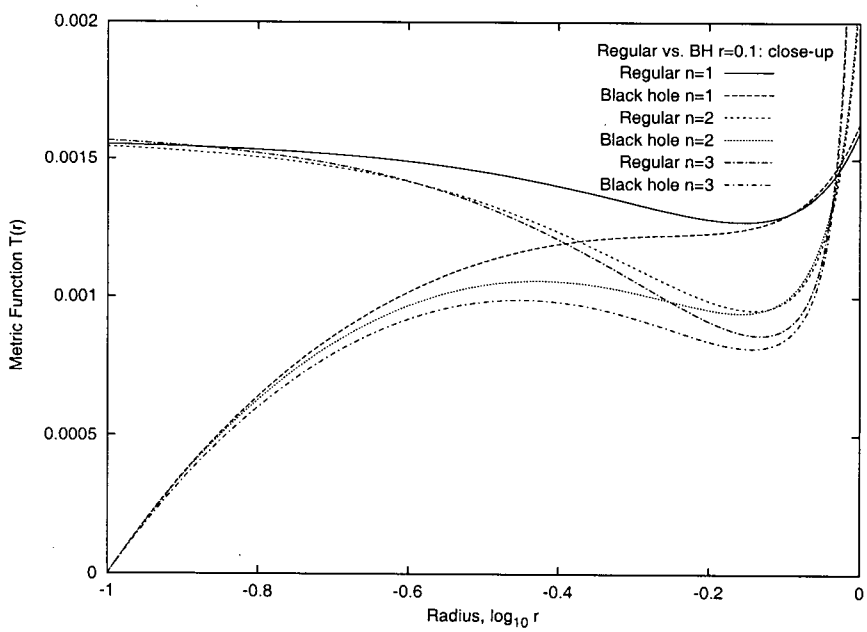

Figure 3.13: Close-up of the first 3 Bartnik-McKinnon and $r_h = 0.1$ black hole solutions near $r = 0$. Only the metric function $T(r)$ is shown. The solutions are normalized to approximately the same $T(0)$ for easier visual comparison.

Table 3.4: Regions of circular orbit stability for different EYM solutions. Last two rows correspond to the Schwarzschild and the extreme Reissner-Nordstrom solutions respectively.

r_h	n	r_{in}	r_{out}	r_{ms}
0.1	1	0.548911	1.01664	6.8524
0.2	1	0.558543	1.01023	7.172
0.3	1	0.644039	0.994828	7.37279
0.4	1	0.742905	0.980872	7.50494
0.5	1	0.838215	0.894269	7.88293
0.51	1	0.859217	0.859217	7.76058
0.1	2	0.695424	0.855577	2.93548
0.1	3	0.723698	0.835827	4.24872
0.1	4	0.725734	0.832823	3.9244
0.1	5	0.724913	0.8316	4.02275
1	1	–	–	9.4867
1	2	–	–	3.72032
1	3	–	–	3.94716
1	4	–	–	4.04562
1	5	–	–	4.03990
0	1	0.700636	1.01743	6.86738
0	2	0.723676	0.860789	2.9806
0	3	0.738857	0.839071	4.16718
0	4	0.746435	0.835575	3.95556
0	5	0.745549	0.838501	4.09606
0	6	0.745404	0.83829	4.06724
0	7	0.745381	0.838257	4.03937
1	*Schw*	–	–	6.0
1	*ERN*	–	–	4.0

While the black-hole solutions for small r_h are very close to the regular ones for $r > 1$, the situation is very different for small r. The black hole metric function $T(r)$ goes to zero near the horizon, while the regular one remains finite. Figure 3.13 shows the closeup of the metric in the region $r_h < r < 1$ for the black hole solutions with $r_h = 0.1$. The metric functions are rescaled pair-wise to the same value of $T(0)$ to give a clearer picture. The shape of the black hole metric in this region near the horizon gives rise to a new feature: a region of stable circular geodesics where the black hole metric starts curving downward to zero, approximately at $r < 1$. This region ends when the shape of the metric starts curving upwards, near $r = 0.55$. Table 3.4 lists the radii of stable circular orbits for different solutions. One can see that the additional island of stable orbits start at r_h below about 0.51 and spans increasingly larger range or radii.

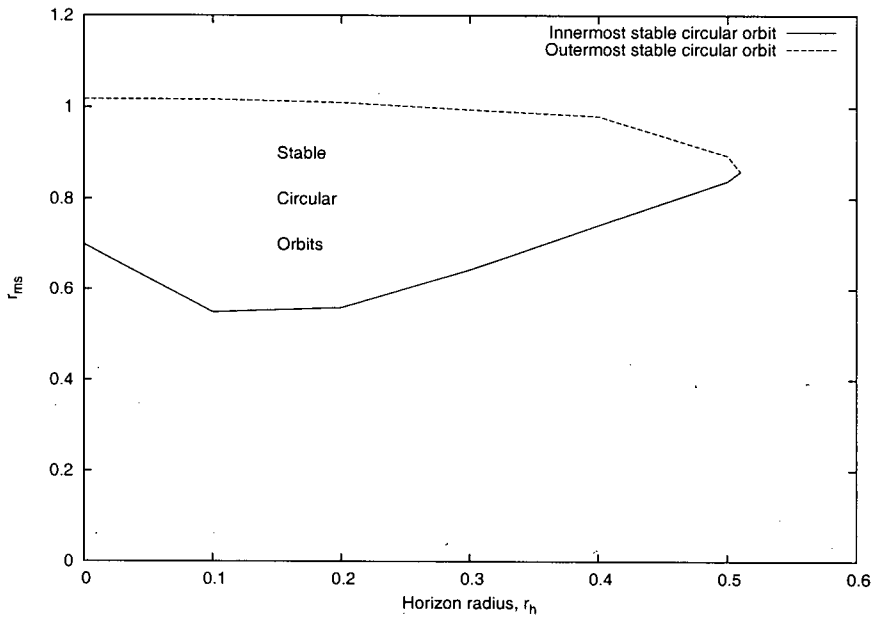

Figure 3.14: Region of stability of circular orbits near the horizon of $n = 1$ EYM black holes with small r_h.

Figure 3.14 shows the range of stable orbit in the island of stability near the horizon vs. the horizon radius.

It is worthwhile to discuss null geodesics near Einstein-Yang-Mills black holes before proceeding to calculate accretion disk spectra. Figures 3.15,3.17,3.19,3.21,3.25 show null geodesics in Schwarzschild, extreme Reissner-Nordstrom, EYM with $r_h = 1, n = 1$, EYM with $r_h = 0.1, n = 1$ and Bartnik-McKinnon with $n = 1$ metrics. Figure 3.22 zooms in on the geodesics that reach the inner ring of stable circular timelike orbits. The general shape of the null geodesics in EYM metric is similar to that of Schwarzschild, and so the outer disk appearance is quite similar. Figures 3.16, 3.18, 3.20, 3.23, 3.26 show images of a thin, non-inclined ring near innermost stable orbit (of the "main" disk) for the Schwarzschild, extreme Reissner-Nordstrom, EYM with $r_h = 1, n = 1$, EYM with $r_h = 0.1, n = 1$ and Bartnik-McKinnon with $n = 1$ metrics. The ring's axis is inclined at 30° relative to the direction towards the observer. The inner ring is located rather deep in the "gravity well", with $g_{00} = 0.01...0.8$, depending on the solution number, and so only the light emitted close to the direction away from center can escape to infinity. In our simulations we extend the null geodesics from infinity toward the disk, so only the subset of null geodesics that escapes to infinity is generated, and all those hit the disk at a steep angle, as shown on figure 3.22. In terms of disk image this corresponds to an impact parameters much larger than the ring radius. This can be seen on figure 3.24, which shows the image of the inner stable ring only. The smaller and wider circle with impact parameter $b \approx 2$ corresponds to the light hitting the disk with a deflection angle $\theta < \pi$ and the larger and narrower circle corresponds to the light deflected between π and 2π. There are no other images, as the

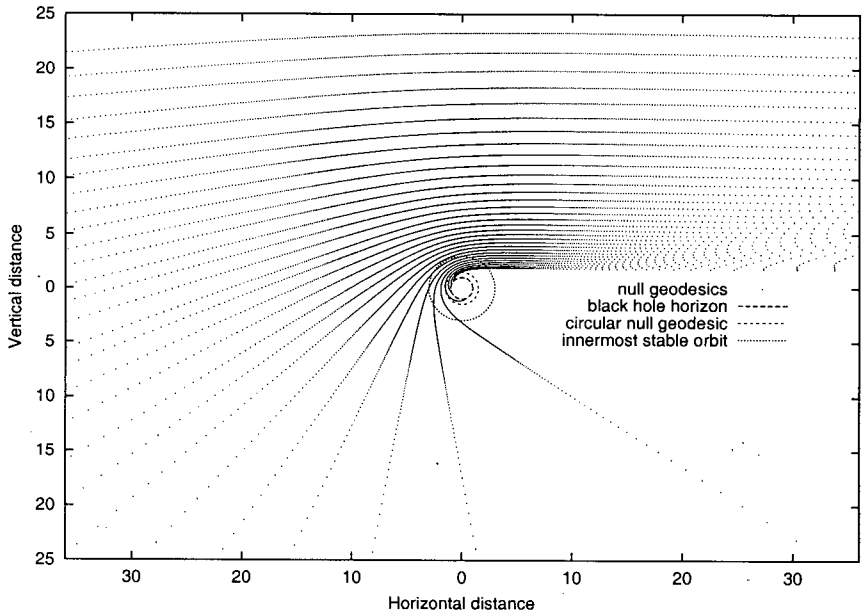

Figure 3.15: Null geodesics for Schwarzschild metric. Concentric circles denote the horizon radius and the innermost stable circular timelike geodesic.

ring is located too far away from the horizon, and the geodesics deflected by $\theta > 2\pi$ pass inside the ring. The situation for the Bartnik-McKinnon solution is even more peculiar. Since this solution is regular, null geodesics can pass through the center $r = 0$ and go back out. While it is unclear what would happen to an accreting object of this type, we include both the geodesics and the ring images of the regular solution, for completeness.

3.5 EYM Line Profile Results

In this section we present the line profiles computed numerically using the metrics described in the previous section.

Figure 3.27 shows the calculated line profiles for the EYM black holes with $r_h = 1$, as well as Schwarzschild and extreme Reissner-Nordstrom, for comparison. The emissivity power law index is $p = 2$, which gives approximately equal weight to inner and outer layers of the disk. The outer disk radius is set to a $r_{out} = 30$, which is shorter than the long-range changes in the metric function $T(r)$ shown on figure 3.7. One can see that the line profile is wider than Schwarzschild already at $n = 1$, and is redshifted for $n = 2, 3, 4$, then converges to extreme Reissner-Nordstrom for $n = 5$. Interestingly, the line profiles for the solutions $n = 3$ and $n = 4$ are similar in the shape to the $n = 1$ and Schwarzschild, but are redshifted by a factor of about 1.5, even though all these solutions have approximately the same ADM mass, and so in the EYM case the frequency shift of the main peak is not a reliable indicator of the black hole mass. The reasons for this behavior can be seen from

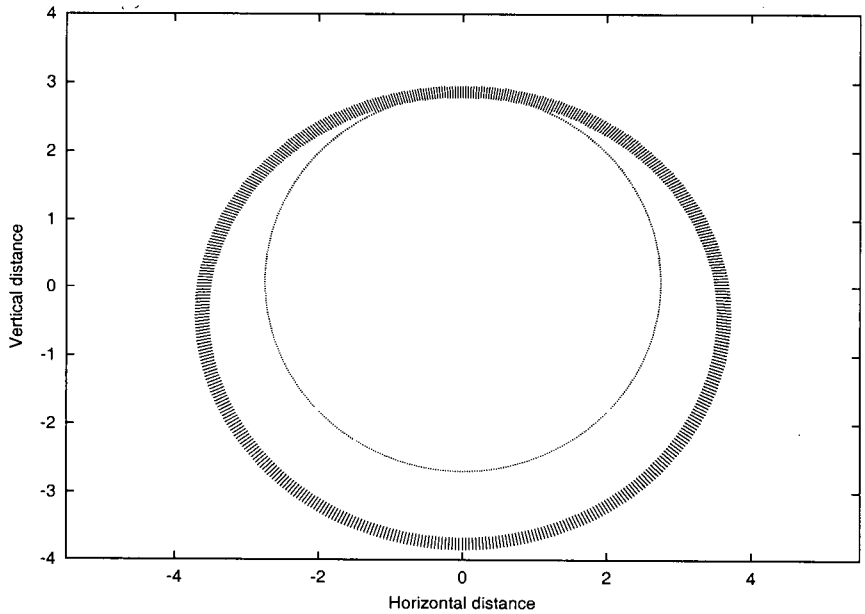

Figure 3.16: Thin ring image for the Schwarzschild metric with $r_h = 1$. Ring inclination is $i = 30°$. Actual inner ring radius $r_{ms} = 3$, apparent ring radius is $b \approx \sqrt{27/2}$. Note the secondary image of the ring at $b = \sqrt{27/4}$.

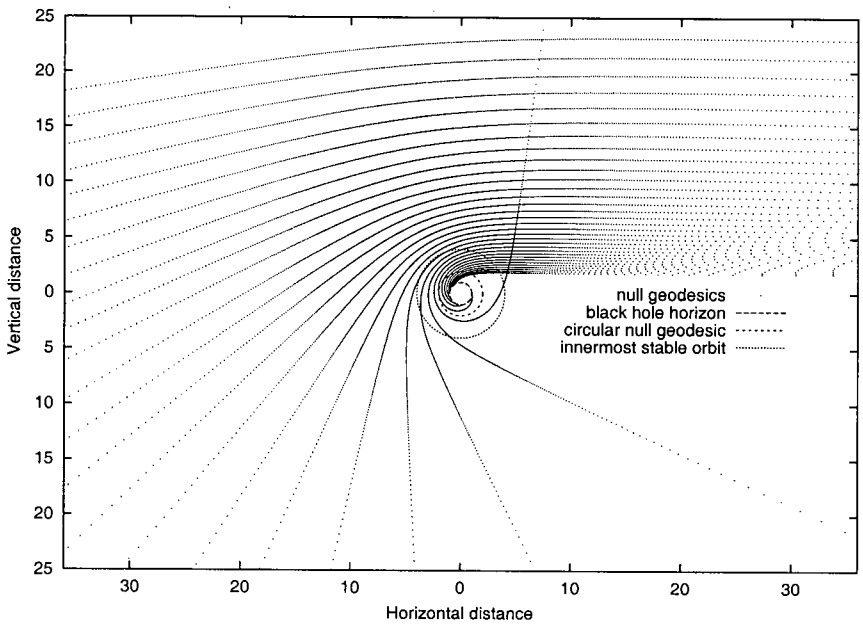

Figure 3.17: Null geodesics for the extreme Reissner-Nordstrom metric. Concentric circles denote the horizon radius and the innermost stable circular timelike geodesic.

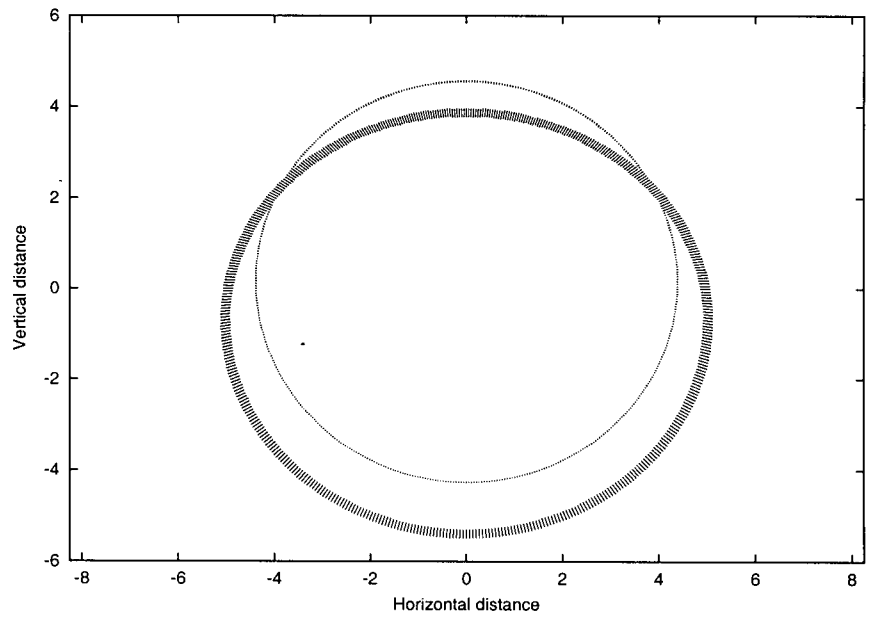

Figure 3.18: Thin ring image for the extreme Reissner-Nordstrom metric with $r_h = 1$. Actual inner ring radius is $r_{ms} = 4$. Ring inclination is $i = 30°$.

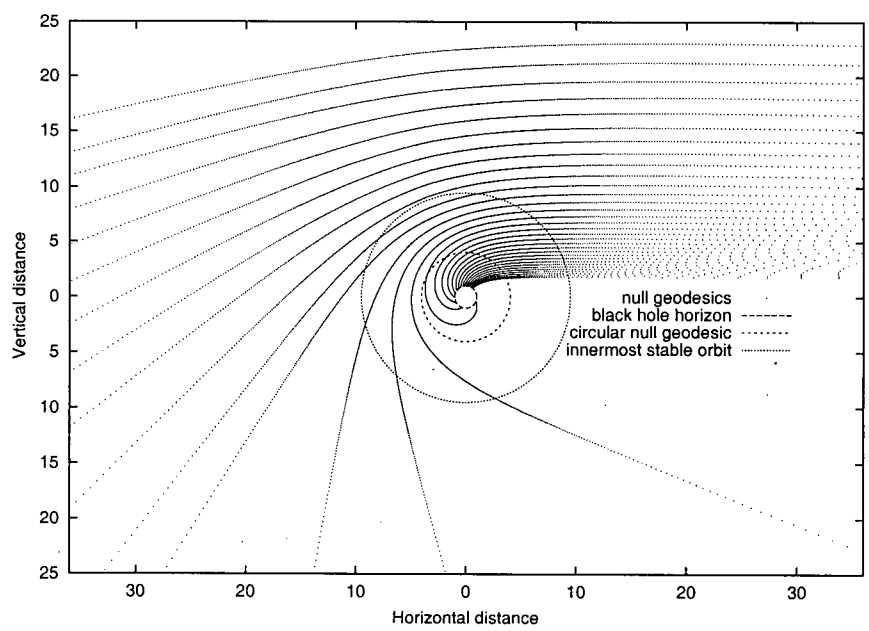

Figure 3.19: Null geodesics for EYM metric with $r_h = 1$, $n = 1$. Concentric circles denote the horizon radius and the innermost stable circular timelike geodesic.

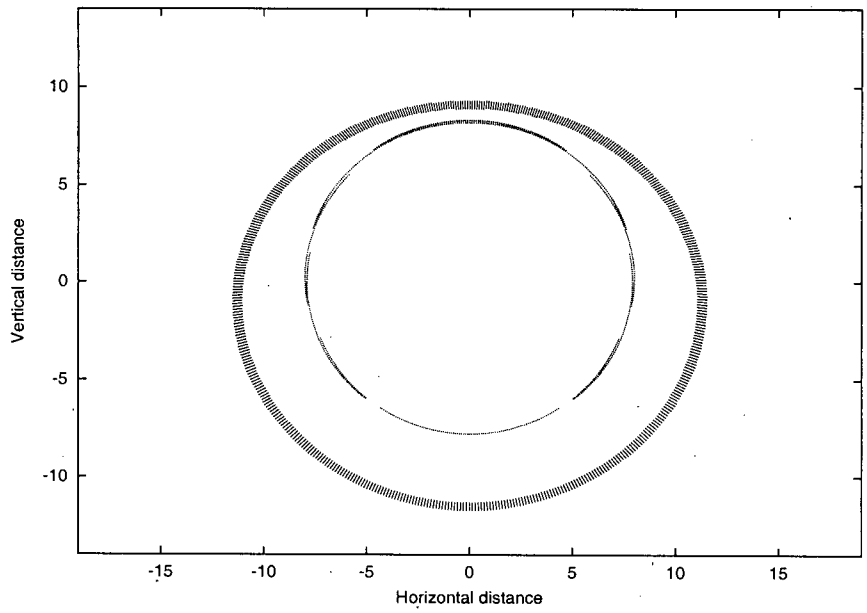

Figure 3.20: Thin ring image for the EYM metric with $r_h = 1$, $n = 1$. Actual inner ring radius is $r_{ms} = 9.49$. Ring inclination is $i = 30°$.

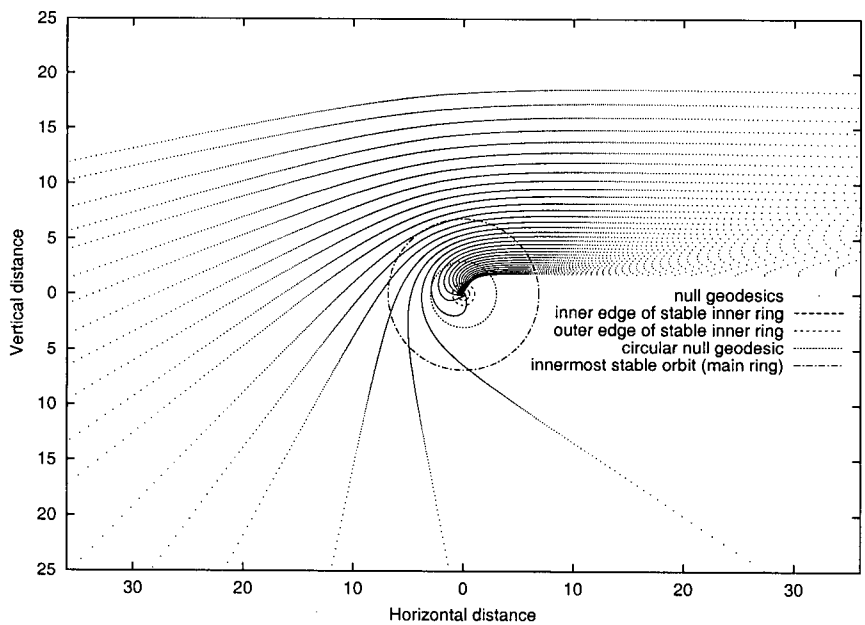

Figure 3.21: Null geodesics for EYM metric with $r_h = 0.1$, $n = 1$. Concentric circles denote the horizon radius and the innermost stable circular timelike geodesic, as well as the innermost stable circular orbit for the outer disk.

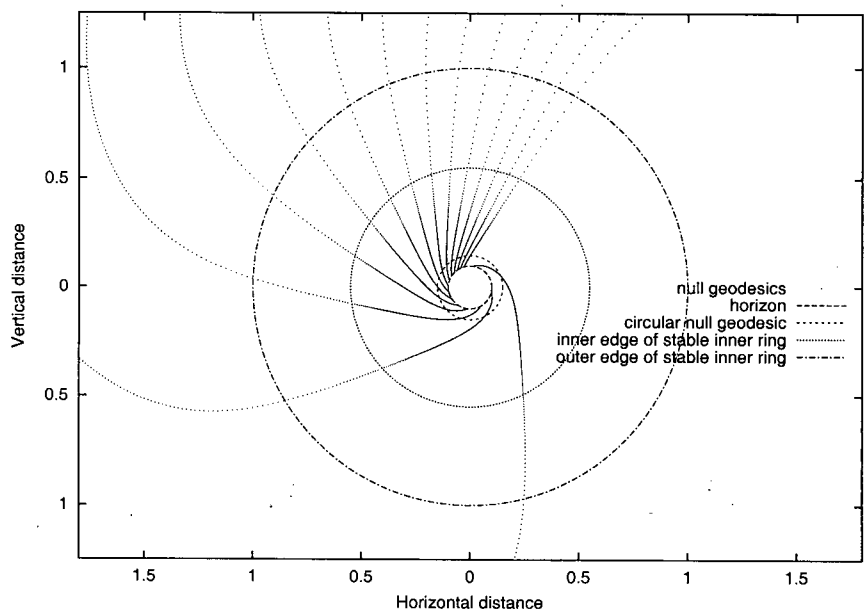

Figure 3.22: Closeup of null geodesics for EYM metric with $r_h = 0.1$, $n = 1$. Concentric circles denote the horizon radius and the innermost stable circular timelike geodesic for the inner ring.

the shape of $T(r)$: For $n = 1$ the metric function $T(r)$ and its slope (which determines the relativistic beaming term through the linear orbital velocity of a timelike circular geodesic $v = \sqrt{rT'/2}$) varies more than that of Schwarzschild between the inner edge of the disk at $r_{ms} \approx$. 9.5 and its outer edge at $r_{out} = 30$. For $n = 2$ the variations are even bigger, and for $n = 3, 4$ the part of the metric within the disk limits look similar to Schwarzschild, but redshifted, more so for $n = 3$ than for $n = 4$. For $n = 5$ the metric is very close to the extreme Reissner-Nordstrom, and so is the line profile. While the radial metric function $g_{rr} = R(r)$ does affect the line profile through its effect on the null geodesics, it is very close to that of the extreme Reissner-Nordstrom even for small n, and so its contribution is not significant.

Figure 3.28 shows line profile for a very wide disk, $r_{out} = 3000$, which spans all interesting metric features for most n. One can see that the profiles are generally very broad. Whenever the disk range includes two phases of the steep slope in $T(r)$, such as for $n = 3$, the profile shows two sets of double peaks, one for each phase.

Similar effects can be seen on figure 3.29 where the emissivity power law exponent is set to a more realistic $p = 3$. This steeper power law causes the power in the spectrum to be skewed toward higher redshifts, produced by the inner layers of the accretion disk.

We now examine the accretion disk line profiles produced by the black holes with smaller horizon radius, first including the outer disk only. Figure 3.30 shows the calculated line profiles for the $n = 1 \ldots 5$ EYM black holes with $r_h = 0.1$. Here again we see that the profile

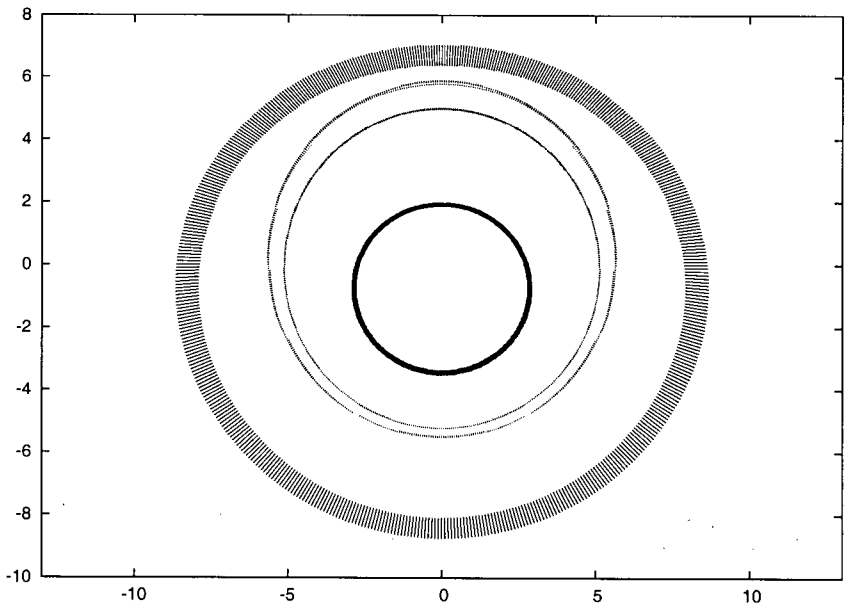

Figure 3.23: Thin ring image for the EYM metric with $r_h = 0.1$, $n = 1$. Images of both the inner stable ring at $r = 0.55\ldots1.01$ and the outer ring near $r_{ms} = 6.85$ are shown. Ring inclination is $i = 30°$. The innermost and the outermost images are primary, the two thin images are secondary. Note that the secondary image of the inner ring is outside the primary one. The x and y axes show horizontal and vertical distance.

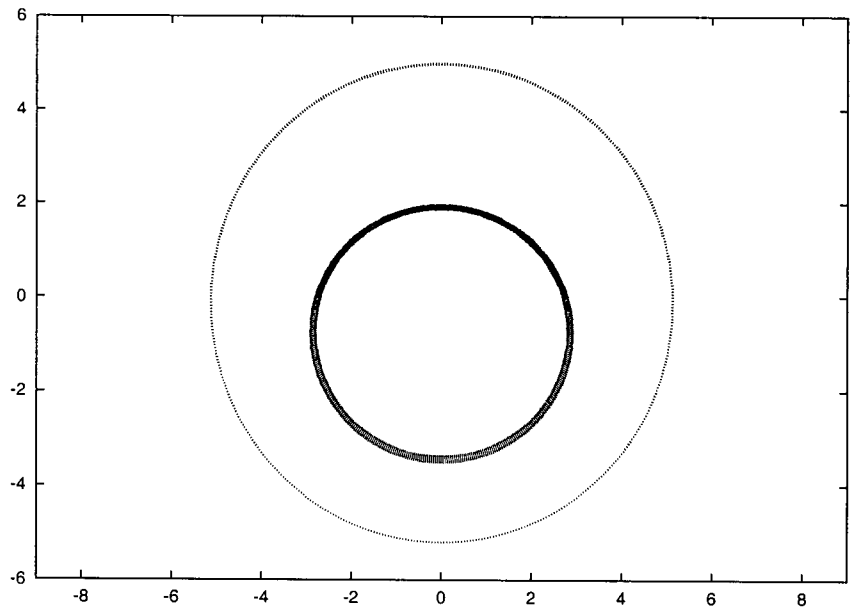

Figure 3.24: Thin ring image for the EYM metric with $r_h = 0.1$, $n = 1$ of the inner stable ring at $r = 0.55\ldots1.01$ only. Ring inclination is $i = 30°$. The x and y axes show horizontal and vertical distance. The x and y axes show horizontal and vertical distance.

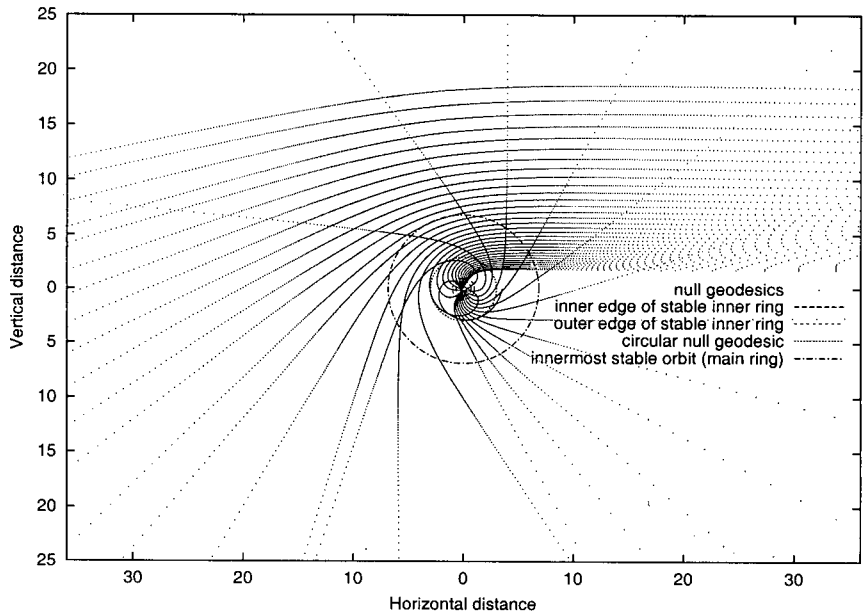

Figure 3.25: Null geodesics for the Bartnik-McKinnon metric with $n = 1$. Concentric circles denote the horizon radius and the innermost stable circular timelike geodesic. Note the geodesics passing through the center $r = 0$.

is largely determined by the shape of the metric function $T(r)$ within the boundaries of the accretion disk.

The above spectrum did not include the emission from the island of stable circular orbits near the horizon, or any emission coming from the region between this inner stable ring and the outer disk, where no stable orbits exist. We neglect any possible contribution from this region, as it is likely to be small and would heavily depend on the particular model of the disk's magnetohydrodynamics. Line profiles shown on figure 3.31 include only the contribution from the inner stable ring, without any contribution from the outer disk. One can see the new feature contributed by this inclusion: a two-peak profile at a redshift of about 30. The high redshift is due to $T(r)$ being very small in this region, corresponding to the "deep gravitational well" the emitted light has to climb out of to reach the observer. Higher solution number n means lower $T(r)$ near the inner disk and bigger redshift of the line profile. This also determines that the total power received by a remote observer from the inner disk will be a tiny fraction of the power received from the outer disk. Figure 3.32 shows the line profile for $n = 1$ when both the inner ind the outer disks are included. The outer disk is made into a thin ring with its width 100 times smaller than its radius, in order to see the inner disk's contribution on the same plot.

For completeness, we also show line profiles from the Bartnik-McKinnon solutions in comparison with the black hole solutions with small horizon radii. Figure 3.33 shows the profiles for the first five such pairs. One can see that in most cases the profiles are quite close, except for the 10% difference in overall redshift for $n = 5$.

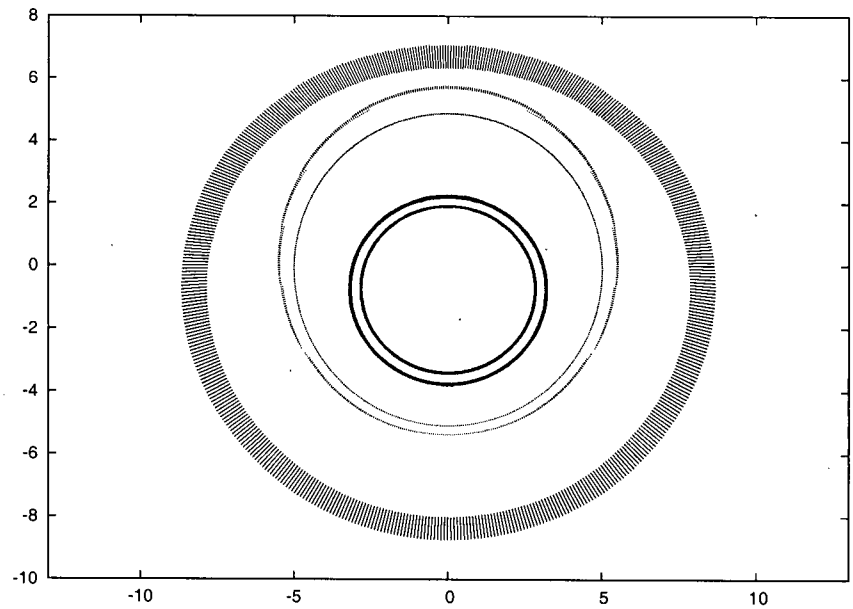

Figure 3.26: Thin ring image for the Bartnik-McKinnon metric with $n = 1$. This is similar to the ring image for the black hole metric with small horizon radius, except there is a new image of the inner ring made by the light going through the center $r = 0$. Ring inclination is $i = 30°$. The x and y axes show horizontal and vertical distance.

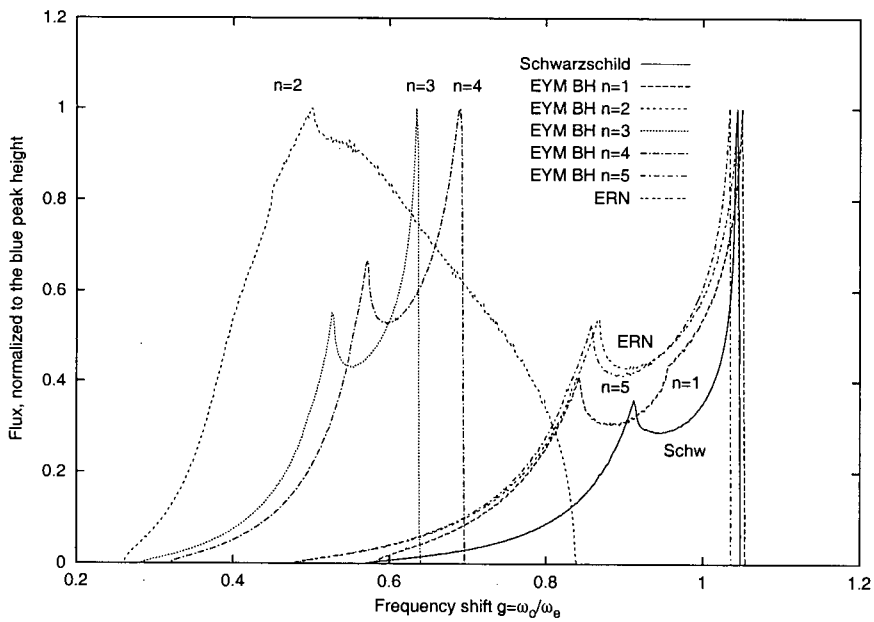

Figure 3.27: Line profiles for EYM $r_h = 1$ black hole accretion disks for different n with the same innermost stable circular orbit r_{in}. The disk parameters are: inclination $i = 30°$, power law exponent $p = 2$, inner radius of the disk $r_{in} = r_{ms}$, outer radius of the disk $r_{out} = 30$.

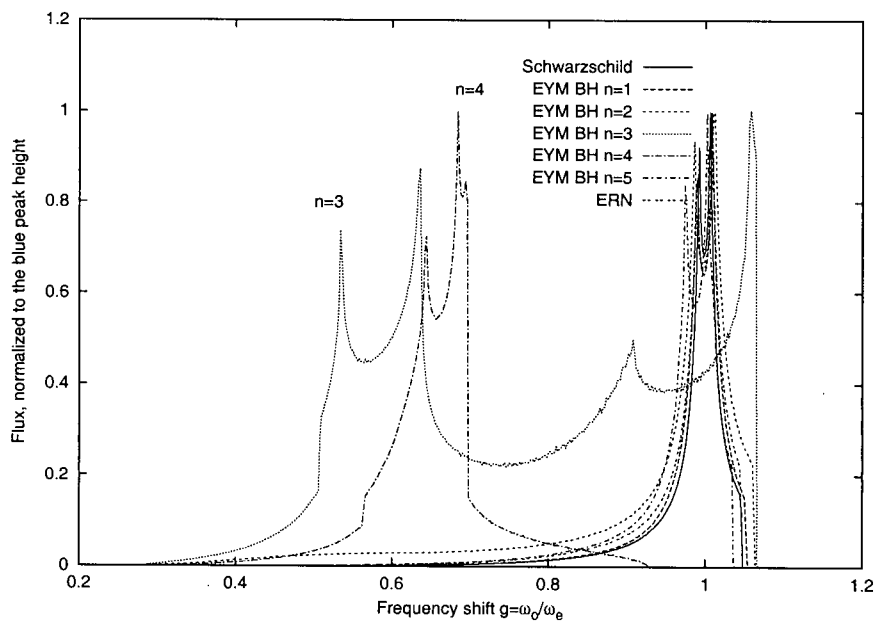

Figure 3.28: Line profiles for EYM $r_h = 1$ black hole accretion disks for different n with the same innermost stable circular orbit r_{in}. The disk parameters are: inclination $i = 30°$, power law exponent $p = 2$, inner radius of the disk $r_{in} = r_{ms}$, outer radius of the disk $r_{out} = 3000$. The $n = 3, 4$ profiles are quite distinct.

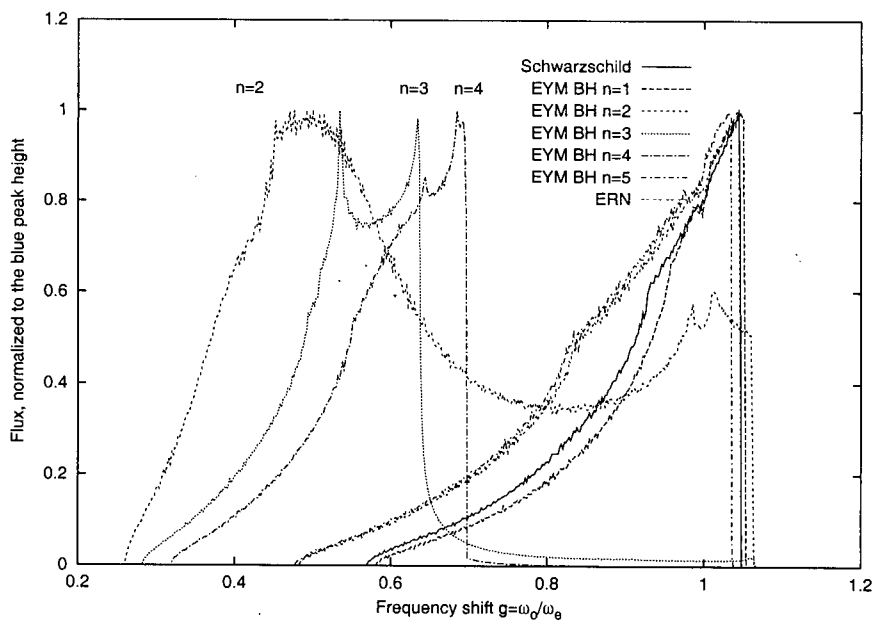

Figure 3.29: Line profiles for EYM $r_h = 1$ black hole accretion disks for different n with the same innermost stable circular orbit r_{in}. The disk parameters are: inclination $i = 30°$, power law exponent $p = 3$, inner radius of the disk $r_{in} = r_{ms}$, outer radius of the disk $r_{out} = 3000$. $n = 2, 3, 4$ profiles are quite distinct, $n = 1$ profile is close to Schwarzschild, $n = 5$ profile is close to extreme Reissner-Nordstrom.

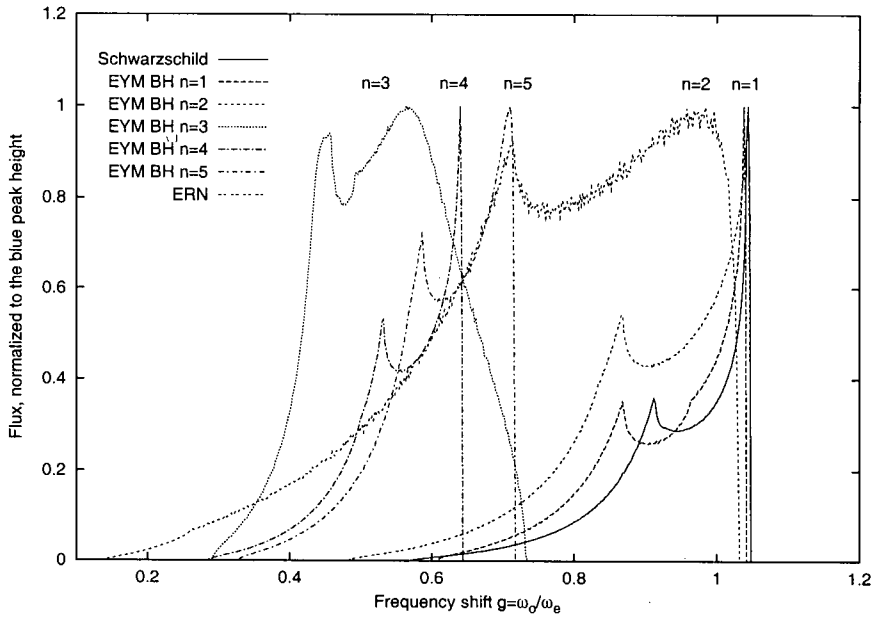

Figure 3.30: Line profiles for EYM black hole accretion disks for $r_h = 0.1$, $n = 1\ldots5$. The disk parameters are: inclination $i = 30°$, power law exponent $p = 2$, inner radius of the disk $r_{in} = r_{ms}$, outer radius of the disk $r_{out} = 30$.

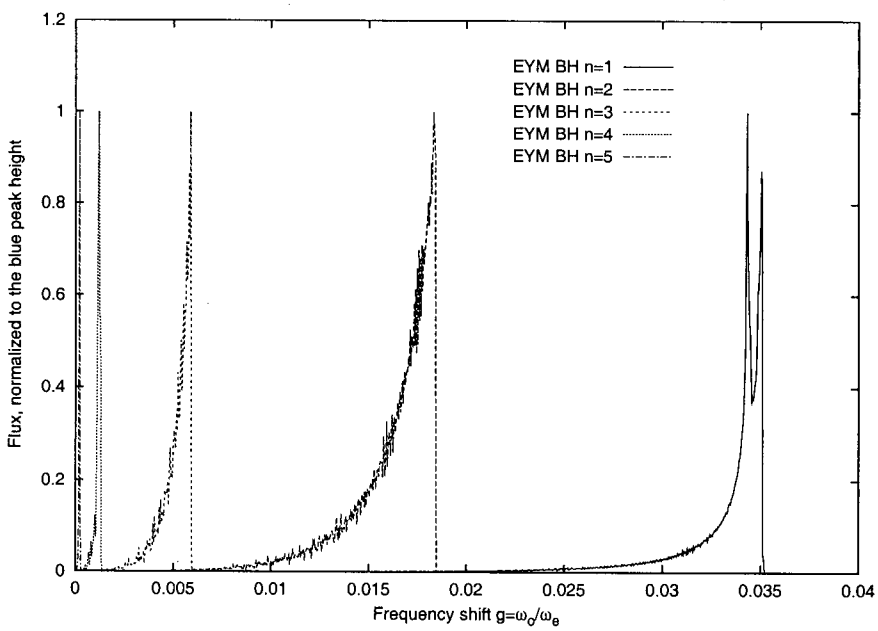

Figure 3.31: Line profiles from the inner accretion disks of EYM black holes with $r_h = 0.1$, $n = 1\ldots5$. The disk parameters are: inclination $i = 30°$, power law exponent $p = 2$, inner radius of the disk $r_{in} = 0.55$, outer radius of the disk $r_{out} = 1.01$.

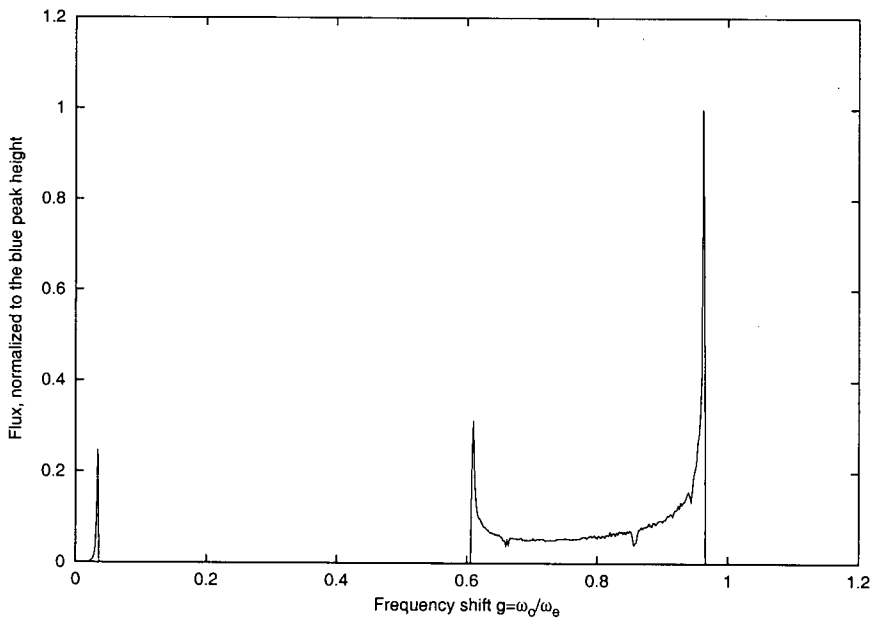

Figure 3.32: The line profile from both the inner and the outer disks from an EYM black hole with $r_h = 0.1$ and $n = 1$. The disk parameters are: inclination $i = 30°$, power law exponent $p = 2$, inner radius of the stable ring near horizon is $r_{in} = 0.55$, outer radius of the ring $r_{out} = 1.01$. The outer disk is just a thin ring near $r_{ms} = 6.85$ to allow the contribution from the inner disk to be noticeable.

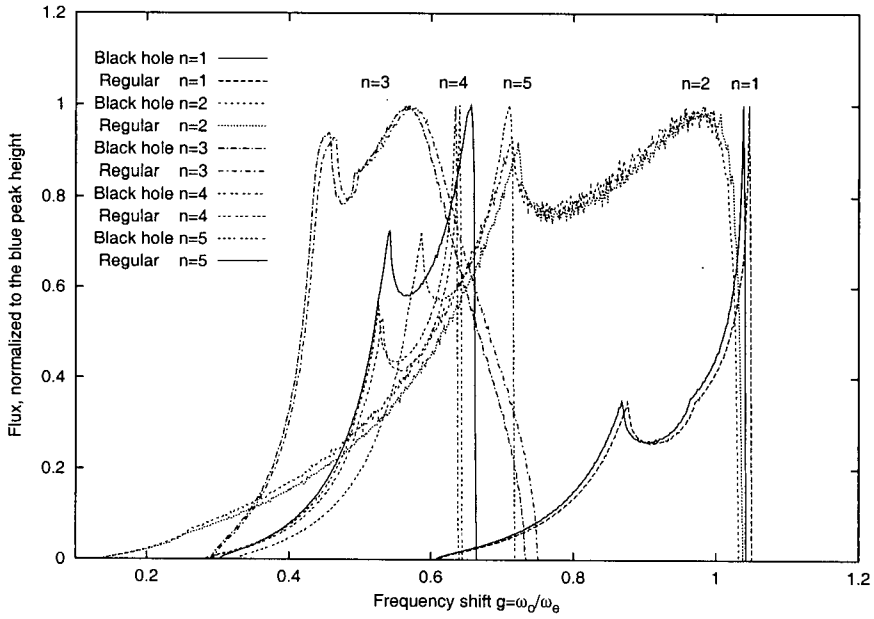

Figure 3.33: Line profiles for both Bartnik-McKinnon and black hole $r_h = 0.1$ solutions for $n = 1\ldots5$. The disk parameters are: inclination $i = 30°$, power law exponent $p = 3$, inner radius of the disk $r_{in} = r_{ms}$, outer radius of the disk $r_{out} = 3000$

3.6 EYM Line Profile Discussion

We numerically constructed the static spherically symmetric solutions of the Einstein equations coupled to the Yang-Mills field and modeled the line profiles from idealized accretion disks around them for different solutions numbers n. We found that the line profile from an EYM metric can be significantly different from that of Schwarzschild or the extreme Reissner-Nordstrom, which is the limiting case of EYM for large n. The profile is generally wider and heavily dependent on both the disk boundaries and the solution number. The full width of the line is determined by the inner parts of the disk, with the part of the disk coming toward the observer providing the blue end and the parts moving away providing the red end of the line profile. For a disk with 90° inclination, the maximum line width is determined by the magnitude of the term $\frac{b}{r}\sqrt{rT'(r)/2}$ for the innermost stable circular orbit. In the literature, only the Schwarzschild and Kerr metrics are commonly considered. In the Schwarzschild case $r = 6M$, $b = \frac{r}{\sqrt{1-\frac{2M}{r}}} = 3\sqrt{6}$, and so the ratio of the highest and lowest frequencies in the line profile is at most a factor of 3, whereas for the extreme Kerr metric with angular momentum $a = 0.998$ this spread can be as large as 7 or 8 (see e.g. [7] for examples), due to the innermost stable circular orbit being much closer to the horizon. What we have shown is that the line width in the EYM case can be as small as that of Schwarzschild or as large or larger than that of Kerr. The shape of the line can be significantly different, and may include an extra pair of peaks redshifted by a factor of two

or so. For solutions with $n = 3, 4$ the line shapes can mimic those of Schwarzschild black hole, albeit significantly redshifted. Thus one cannot reliably determine the mass of such EYM black hole from the position of the blue peak alone.

EYM BH metrics for large solution number n look progressively more like a maximally-charged RN solution, especially near the inner disk, and since for a large emission power law exponent most of the line profile features come from this area, the spectra become progressively more similar to those of ERN.

For black holes with the horizon radius $r_h << 1$ there is an island of stable orbits around $r = 0.5...1.1$. Whether any emission from this area will be detectable would depend on the dynamics of the disk. Assuming the infalling matter follows the circular geodesics Emission from a disk in this area has a familiar 2-peak shape, but is red-shifted by a factor of 30 or more, depending on solution number. One could conceivably try to detect these EYM black holes by correlating the observed emissions near the main line (6.4keV for iron K_α) with those at about 1 to 3% of this energy. This maybe rather difficult, as this feature is much weaker and it is in the noisier part of the spectrum and it can be masked by or confused with other processes emitting in the same part of the spectrum.

Bibliography

[1] A.C.Fabian, K. Iwasava, C.S. Reynolds, and A.J. Young. *PASP*, 112:1145, 2000.

[2] R. Bartnik and J. Mckinnon. Particle - like solutions of the einstein yang-mills equations. *Phys. Rev. Lett.*, 61:141–144, 1988.

[3] P. Breitenlohner, P. Forgacs, and D. Maison. Static spherically symmetric solutions of the einstein-yang-mills equations. *Communications in Mathematical Physics*, 163(1):141–72, 1994.

[4] K. Chen and D. Eardley. *ApJ*, 382:125, 1991.

[5] K. Chen, J.P. Halpern, and A.V. Filippenko. *ApJ*, 339:742, 1989.

[6] C.T. Cunningham. *ApJ*, 202:788, 1975.

[7] Y. Dabrowski, A. C. Fabian, K. Iwasawa, A. N. Lasenby, and C. S. Reynolds. The profile and equivalent width of the x-ray iron emission-line from a disk around a kerr black hole. 1997.

[8] A. C. Fabian, M. J. Rees, L. Stella, and N. E. White. X-ray fluorescence from the inner disc in cygnus x-1. *Mon. Not. Roy. Astron. Soc.*, 238:729–736, 1989.

[9] C. Fanton, M. Calvani, F. de Felice, and Andrej Cadez. *PASJ*, 49:159, 1997.

[10] G. W. Gibbons and S. W. Hawking. Cosmological event horizons, thermodynamics, and particle creation. *Phys. Rev.*, D15:2738–2751, 1977.

[11] Stephen Hawking. Gravitationally collapsed objects of very low mass. *Mon. Not. Roy. Astron. Soc.*, 152:75, 1971.

[12] Markus Heusler. Stationary black holes: Uniqueness and beyond. *Living Rev. Rel.*, 1:6, 1998.

[13] Burkhard Kleihaus, Jutta Kunz, and Abha Sood. Charged su(n) einstein-yang-mills black holes. *Phys. Lett.*, B418:284–293, 1998.

[14] Martin Kunz, Pier-Stefano Corasaniti, David Parkinson, and Edmund J. Copeland. Model-independent dark energy test with sigma(8) and t(0) using wmap. 2003.

[15] Ari Laor. Line profiles from a disk around a rotating black hole. IASSNS-AST-91-2.

[16] George V. Lavrelashvili and Dieter Maison. A remark on the instability of the bartnik-mckinnon solutions. *Phys. Lett.*, B343:214–217, 1995.

[17] J.-P. Luminet. *Astron. Astrophys.*, 75:228, 1979.

[18] C.W. Misner, K.S. Thorne, and J.A. Wheeler. *Gravitation.* Freeman, San Francisco, 1973.

[19] W. H. Press, S. A. Teukolsky, W. T. Vetterling, and B. P. Flannery. *Numerical Recipes in C, The art of Scientific Computing.* Second edition, 1997.

[20] J. A. Smoller and A. G. Wasserman. Extendability of solutions of the einstein-yang-mills equations. *Commun. Math. Phys.*, 194:707–732, 1998.

[21] J. A. Smoller, A. G. Wasserman, and S. T. Yau. Existence of black hole solutions for the einstein / yang- mills equations. *Commun. Math. Phys.*, 154:377–401, 1993.

[22] J. A. Smoller, A. G. Wasserman, S. T. Yau, and J. B. McLeod. Smooth static solutions of the einstein yang-mills equations. *Commun. Math. Phys.*, 143:115–147, 1991.

[23] Z. Stuchlik and S. Hledik. Some properties of the schwarzschild-de sitter and schwarzschild - anti-de sitter space-times. *Phys. Rev.*, D60:044006, 1999.

[24] Zdenek Stuchlik, Stanislav Hledik, Jiri Soltes, and Erlend Ostgaard. Null geodesics and embedding diagrams of the interior schwarzschild-de sitter spacetimes with uniform density. *Phys. Rev.*, D64:044004, 2001.

[25] Y. Tanaka et al. Gravitationally redshifted emission implying an accretion disk and massive black hole in the active galaxy mcg:-6-30- 15. *Nature*, 375:659, 1995.

[26] Mikhail S. Volkov and Dmitri V. Gal'tsov. Gravitating non-abelian solitons and black holes with yang- mills fields. *Phys. Rept.*, 319:1–83, 1999.

Appendix A

Appendix

A.1 Circular Time-like Orbits

In this section we derive the equations for the circular orbits in an arbitrary static spherically-symmetric metric, then investigate the stability of such orbits and the restrictions they pose on the Keplerian disk. The metric we deal with exclusively is

$$ds^2 = -T(r)dt^2 + R(r)^{-1}dr^2 + r^2 d\Omega^2. \tag{A.1}$$

We assume that there exist some finite r_0 such that both $T(r)$ and $R(r)$ are positive for all $r > r_0$. If $T(r_0) = 0$ then the metric describes a black hole with the horizon radius $r_h = r_0$. Since zeros of T(r) correspond to event horizons, only the outermost zero r_0 is relevant from the remote observer's point of view, as no information from $r < r_0$ can be received by this observer. R(r) is in the denominator because usually both T(r) and R(r) have zeros at the same value(s) of r. For the Schwarzschild metric, the unique vacuum solution, $T(r) = R(r) = 1 - \frac{2M}{r}$.

Equation A.1 is a Lagrangian for an action $\int \sqrt{-ds^2}$, since the geodesics are the extrema of the world line. One of the standard ways to proceed is to go from the full 3D picture to radial dependence only, using the conserved charges resulting from the time-invariance and the spherical symmetry of the metric, and then use the effective potential technique to deal with the radial ODE. This approach is implemented below. There are three conserved charges associated with the angular degrees of freedom, corresponding to the conservation of angular momentum. By choosing our coordinates such that initially $\theta = \frac{\pi}{2}$ and $d\theta = 0$, we can eliminate the θ coordinate altogether, as the $d\theta = 0$ condition is preserved by the equations of motion (orbits are planar). Defining proper time τ as $d\tau^2 = -ds^2$, we write the equation of motion for ϕ

$$\frac{d}{d\tau}\frac{d\phi}{d\tau} = 0, \tag{A.2}$$

This can be integrated to

$$\frac{d\phi}{d\tau} = l, \tag{A.3}$$

where $l = const$ is a conserved charge with the meaning of angular momentum per unit mass. It has dimension of length in the geometerized units. Similarly, the conserved charge due to staticity of the metric is energy e (dimensionless in out units):

$$T(r)\frac{dt}{d\tau} = e. \tag{A.4}$$

Eliminating both t and ϕ from the metric equation (1.3) using (A.3) and (A.4), we are left with the radial equation of motion:

$$d\tau^2 = e^2\frac{d\tau^2}{T(r)} - R(r)^{-1}dr^2 - \frac{l^2}{r^2}d\tau^2, \tag{A.5}$$

or, equivalently,

$$(\frac{dr}{d\tau})^2 + V_{eff} = 0, \tag{A.6}$$

where

$$V_{eff} = R(r)(-\frac{e^2}{T(r)} + 1 + \frac{l^2}{r^2}), \tag{A.7}$$

is the effective potential of our now effectively one-dimensional problem. The properties of this potential as a two-parameter (e, l) family of functions determine the behavior of the time-like geodesics. The extrema of the effective potential correspond to the circular orbits. This yields two conditions

$$V_{eff}(r) = 0, V'_{eff}(r) = 0, \tag{A.8}$$

which determine the orbit parameters e and l as functions of the circular orbit radius r:

$$\begin{aligned} l_{circ}(r) &= r\sqrt{\frac{\frac{rT'}{2}}{T - \frac{rT'}{2}}}, \\ e_{circ}(r) &= T\sqrt{1 + \frac{l^2}{r^2}}. \end{aligned} \tag{A.9}$$

Here T' is defined as $\frac{dT(r)}{dr}$ and the dependence on r is assumed. Note that there is no dependence at all on the radial function R(r) for the circular orbit parameters. If the equations (A.9) are not defined for some r (the argument of the square root is negative), then there are no circular orbits for these radii.

Now we substitute (A.9) in the 4-velocity $u^a = \frac{e}{T}t^a + \frac{l}{r^2}\phi^a$ of the time-like circular geodesic at a distance r:

$$u^a = \frac{1}{\sqrt{T - rT'/2}}(t^a + \frac{1}{r}\sqrt{\frac{rT'}{2}}\phi^a), \tag{A.10}$$

where t^a and ϕ^a are the coordinate basis vectors and the term $\frac{1}{\sqrt{T-rT'/2}}$ comes from the normalization condition $u^2 = -1$.

There are two expressions in the equations (A.9) and (A.10) which deserve their own names:

$$v = \sqrt{\frac{rT'}{2}}, \tag{A.11}$$

which is the linear orbital velocity of the emitter, and

$$\gamma = (T - v^2)^{-\frac{1}{2}}, \tag{A.12}$$

which reduces to the familiar $\gamma = (1 - v^2)^{-\frac{1}{2}}$ in flat spacetime. We can now recognize in the expression for the 4-velocity (A.10) the analog of the Lorentz transformation in curved spacetime in polar coordinates:

$$u^a = \gamma(t^a + v\frac{1}{r}\phi^a). \tag{A.13}$$

For convenience, this derivation was done in disk coordinates (t', r', θ', ϕ'). To transform to the observer's coordinates (t, r, θ, ϕ), we need to rotate the 4-velocity by the angle i in the x-z plane, leading to the equation (1.4).

To find out which circular orbits are stable, we need to find all r at which V_{eff} has a minimum at the values of l and e given by (A.9). This leads to the following inequality:

$$(\frac{\gamma}{v})^2(3T'T - 2rT'^2 + rTT") > 0. \tag{A.14}$$

The term $(\frac{\gamma}{v})^2$ is positive for all circular orbits and can be omitted (one still has to consider only the domain where circular geodesics exist), so we get

$$1 - \frac{2rT'}{3T} + \frac{rT"}{3T'} > 0. \tag{A.15}$$

We recover the familiar expression $r_{ms} = 6M$ for the Schwarzschild metric $T = 1 - \frac{2M}{r}$.

A.2 Null Geodesics

We need null geodesics to calculate the trajectories the emitted light travels until it reaches the observer. There are several possible outcomes when light is emitted from the disk: it can reach the remote observer, or it can disappear inside the horizon, or it can hit the disk and, depending on the disk model, either get absorbed (optically-thick disk) or pass through unchanged (optically-thin disk). We will see that the difference in the spectral line due to the optical properties of the disk is small in most cases, because only a small fraction of the emitted light hits the disk.

The equation of a null geodesic can be derived the same way as the equation of a time-like geodesic (A.5), except on the left-hand side ds^2 is zero:

$$0 = e^2\frac{d\tau^2}{T(r)} - R(r)^{-1}dr^2 - \frac{l^2}{r^2}d\tau^2. \tag{A.16}$$

Here τ is no longer proper time (which is zero by definition of null geodesic), but just an affine parameter. Solving for $\frac{dr}{d\tau}$ gives, as before, an expression for the effective potential:

$$V_{eff} = R(r)(\frac{l^2}{r^2} - \frac{e^2}{T(r)}), \tag{A.17}$$

Due to conformal reparameterization freedom on τ, only the ratio $\frac{l}{e}$ is an independent parameter, so we now have a one-parameter family of functions for V_{eff}:

$$V_{eff} = \frac{R(r)}{T(r)}(\frac{b^2}{r^2}T(r) - 1), \tag{A.18}$$

where $b = \frac{l}{e}$ is the photon impact parameter that completely determines the null geodesic, up to spatial rotations. The following is the 4-momentum of a null geodesic in the same coordinates as before:

$$p^a = h\nu(\frac{1}{T}t^a + \sqrt{\frac{R}{T} - R(\frac{b}{r})^2}r^a + \frac{b}{r^2}\theta^a). \tag{A.19}$$

A.3 EYM Equations in log scale

We rewrite the equations for the spherically-symmetric static EYM metric after switching to the new radial coordinate $x = \ln(r)$. For convenience, in the following all the derivatives are by x, but r is still retained as a shorthand for e^x.

First and second derivatives:

$$A'(r) = A'(x)/r \tag{A.20}$$

$$w'(r) = w'(x)/r \tag{A.21}$$

$$w"(r) = (w"(x) - w'(x)^2)/r^2. \tag{A.22}$$

The EYM equations in the new coordinates are now

$$A' + \frac{2Aw'^2}{r^2} = \frac{\Phi}{r}$$

$$Aw" - Aw' + \frac{\Phi\ w'}{r} + uw = 0. \tag{A.23}$$